PPARγ mediated enhanced lipid biogenesis fuels *Mycobacterium tuberculosis* growth in a drug-tolerant hepatocyte environment.

Binayak Sarkar[1], Jyotsna Singh[1], Mohit Yadav[1], Priya Sharma[2], Raman Deep Sharma[2], Shweta Singh[3], Aakash Chandramouli[4], Kritee Mehdiratta[5], Ashwani Kumar[3], Siddhesh S. Kamat[4], Devram S. Ghorpade[1], Debasisa Mohanty[1], Dhiraj Kumar[2], Rajesh S. Gokhale[1,4, #]

1 Immunometabolism laboratory, National Institute of Immunology, New Delhi, India, 2 Cellular Immunology Group, International Centre for Genetic Engineering and Biotechnology, New Delhi, India 3 CSIR-Institute of Microbial Technology, Chandigarh, India, 4 Indian Institute of Science Education and Research, Pune, Maharashtra, India.5 Council Of Scientific and Industrial Research–Institute of Genomics and Integrative Biology (CSIR-IGIB), New Delhi 110025, India, Academy of Scientific and Innovative Research (AcSIR), Ghaziabad 201002, India

Current address: Indian Institute of Science Education and Research, Pune, Maharashtra, India.

Keywords: Liver, Mtb, hepatocytes, PPARγ, anti-TB drugs, lipid droplets.

Corresponding author: Rajesh S. Gokhale (rsg@nii.ac.in)

Abstract:

Mycobacterium tuberculosis (Mtb) infection of the lungs, besides producing prolonged cough with mucus, also causes progressive fatigue and cachexia with debilitating loss of muscle mass. While anti-tuberculosis (TB) drug therapy is directed toward eliminating bacilli, the treatment regimen ignores the systemic pathogenic derailments that probably dictate TB-associated mortality and morbidity. Presently, it is not understood whether Mtb spreads to metabolic organs and brings about these impairments. Here we show that Mtb creates a replication-conducive milieu of lipid droplets in hepatocytes by upregulating transcription factor PPARγ and scavenging lipids from the host cells. In hepatocytes, Mtb shields itself against the common anti-TB drugs by inducing drug-metabolizing enzymes. Infection of the hepatocytes in the *in vivo* aerosol mice model can be consistently observed post-week 4 along with enhanced expression of PPARγ and drug-metabolizing enzymes. Moreover, histopathological analysis indeed shows the presence of Mtb in hepatocytes along with granuloma-like structures in human biopsied liver sections. Hepatotropism of Mtb during the chronic infectious cycle results in immuno-metabolic dysregulation that could magnify local and systemic pathogenicity, altering clinical presentations.

Keywords: *Mycobacterium tuberculosis*, PPARγ, anti-TB drugs, lipid droplets.

.

Introduction

Mycobacterium tuberculosis (Mtb), the causative agent of human tuberculosis, remains the leading infectious killer globally with an estimated death of 1.3 million in 2022[1]. Despite progressive work on designing new anti-TB therapeutics and implementing vaccination programs in TB-endemic countries, it has a high global case fatality rate and a poor treatment success rate, along with a rising number of drug-resistant infections[2, 3]. Emerging paradigms in infectious diseases advocate tackling pathogen-driven ailments as one-dimensional problems, where the entire emphasis is given to pathogen elimination. A holistic understanding of how the host systems respond to the infection, vaccination, and treatment is key to TB management programs[4]. Recent widespread and severe physiological derangements associated with COVID-19 patients, even after the elimination of the virus, have brought back the focus on identifying novel strategies that are inclusive of modulating the host immune-metabolic axis[5, 6].

The clinical symptoms of pulmonary TB encompass localized manifestations like prolonged cough with mucus, pleuritic chest pain, hemoptysis, and lung damage. Besides, systemic outcomes like cachexia, progressive fatigue, oxidative stress, altered microbiota and glucose intolerance result in organ-wide disruptions[7, 8]. Pulmonary TB patients often suffer from progressive and debilitating loss of muscle mass and function with severe weight loss, this TB-associated cachexia cannot be reversed by conventional nutritional support[9, 10]. Besides, numerous epidemiological studies indicate that hyperglycemia may occur during active tuberculosis, which can compromise insulin resistance and glucose tolerance, although the mechanisms are unclear[7, 11, 12]. Both the localized and systemic pathophysiology of TB infection indicate an alteration in the

host immuno-metabolic axis. It is somewhat bewildering that the engagement of the liver during the Mtb infection cycle is not considered, despite its central role in balancing the immune and metabolic functions of the body[13]. The crosstalk between the liver and lung has been largely overlooked in tuberculosis (TB), even though acute phase proteins (APPs) are used as predictive biomarkers in pulmonary tuberculosis[14]. A robust hepatic APR response in mice, mediated by key hepatocyte transcription factors, STAT3 and NF-κB/RelA, has been known to trigger pulmonary host defenses for survival during pneumonia and sepsis[15]. In TB, the active phase of the disease is associated with heightened expression of various genes that modulate flux in the lipid metabolic pathways[16-18].

The liver is involved in a wide variety of functions – synthesis of plasma proteins, secretion of various hepatokines, degradation of xenobiotic compounds, and storage of lipids, glucose, vitamins, and minerals [19, 20]. De-novo lipogenesis, secretion of acute phase proteins, hepatokine production, etc. are all directly or indirectly controlled by the hepatocytes, thereby communicating with almost all the organs of the body[19, 21]. Moreover, the liver is actively involved in triacylglycerol synthesis and storage under the intricate regulation of various hormones like insulin, glucagon, and thyroid hormone[22]. All these functions uniquely position the liver as the central regulator of lipid metabolism. To avert organ damage, the liver maintains tolerogenic properties rendering it an attractive target for various pathogenic microorganisms. Although several studies have indicated the role of both -Mtb virulence components and host factors (immune activation, nitric oxide, IFNγ, intracellular pH and hypoxia) in the generation of Mtb drug tolerance, the role of liver, being the principal center for xenobiotic metabolism needs careful

88 investigation[23-27]. Liver is the hub of both phase I and phase II drug modifying enzymes
89 (DMEs). The levels as well as the activity of both type of DMEs play significant roles in
90 determining the pharmacokinetics and efficacy of various drugs across multiple diseases,
91 from infection to malignancy[28].

92 In this study, we demonstrate the active involvement of the liver in a murine aerosol TB
93 infection model during the chronic phase and establish hepatocytes as a new replicative
94 niche for Mtb. Using a variety of *in vivo*, *ex vivo*, and *in vitro* techniques we show how Mtb
95 perturbs biological functions within hepatocytes remodeling intracellular growth,
96 localization, and drug sensitivity. Cellular and mass spectrometric studies demonstrate
97 Mtb infection-mediated enhanced fatty acid biogenesis and TAG biosynthesis in the
98 hepatocytes regulated by PPARγ. We propose that infection of hepatocytes by Mtb during
99 the chronic phase can contribute to significant changes in disease progression, TB
100 treatment, and development of infection-induced metabolic diseases.

101 **Results**

102 **Human pulmonary tuberculosis patients harbor Mtb in the liver.**

103 Mtb infects lungs, and other organs like lymph nodes, pleura, bones, and meninges.
104 There are also isolated case reports of hepatic TB, without providing many
105 pathophysiological consequences[29, 30]. To gain further insights into the involvement of
106 the liver in Mtb infections, we acquired human autopsied liver samples from individuals
107 with miliary tuberculosis and analyzed them for the presence of Mtb bacilli. Hematoxylin
108 and eosin (H and E) staining showed the presence of distinct immune cell infiltration and
109 granuloma-like structures in the infected samples **(Fig 1A and Fig S1C)**. We examined

110 the liver specimens with Mtb specific Ziehl-Nielsen (Z-N) acid-fast and auramine O-
111 rhodamine B stain (**Fig 1B, C**). Both these stains showed distinct positive signals with
112 characteristic rod-shaped bacilli that could be visualized by the acid-fast staining (as
113 indicated by arrows) **(Fig 1B).** We further corroborated our findings by performing
114 fluorescence in-situ hybridization (FISH) using Mtb-specific 16s rRNA probes, where
115 specific signals were observed **(Fig 1D).** The specific staining in FISH eliminates the
116 possibility of non-tuberculous mycobacteria (NTMs) in the tissue specimen and confirms
117 the presence of Mtb infection in the liver. Similar staining in the uninfected liver sections
118 from other individuals did not show any signal. **(Fig S1 A, B**). Although hepatic granuloma
119 is the characteristic histological feature for both local and miliary forms of hepatic TB, the
120 precise involvement of the different cells like Kupffer cells, hepatocytes, stellate cell, liver
121 sinusoidal endothelial cells, hepatic stellate cells, and other cell types have not been
122 studied in detail[31]. Multiplex immunostaining with β-actin antibody and Mtb-specific
123 Ag85B antibody shows the presence of Ag85B signals within the human hepatocytes
124 further confirming the presence of Mtb within hepatocytes (**Fig 1E and Fig S1D)**,
125 indicated with yellow arrows). Hepatocytes are morphologically distinct, large polygonal
126 cells (20-30 μm) with round nuclei, many of which are double-nucleated and mainly
127 positioned at the center of the cytoplasm[32]. The presence of Ag85B signals near the
128 nucleus, as depicted in (**Fig 1E and S1 D)**, further supports our assertion. Moreover,
129 hepatic granulomas in the human samples showed localized clustering of the immune
130 cells **(Fig S1D).** Furthermore, to establish a correlation between liver Mtb load and Mtb
131 burden at the primary infection site, the lung, we conducted H&E staining and acid-fast
132 staining on lung sections from the same individuals. H&E staining revealed distinct

133 granulomas, while acid-fast staining confirmed an elevated bacterial load, both indicative
134 of a high degree of infection **(Fig S1E, F).** Using auramine O-rhodamine B, Ziehl-Nielsen
135 acid-fast staining, and FISH, Mtb presence was detected in several lung specimens **(Fig**
136 **S1G).** These results indicate Mtb infection in the liver of human subjects and suggest the
137 localization of Mtb within hepatocytes. These findings are quite intriguing considering very
138 few studies have discussed the lung-liver cross talk or the involvement of liver in
139 pulmonary TB.

140 **Mtb infection of mice via the aerosol route leads to significant infection of the liver**
141 **and primary hepatocytes.**

142 To investigate whether the liver harbors Mtb during mice aerosol infection, we infected
143 C57BL/6 mice with 200 CFU of Mtb *H37Rv* and scored for the bacterial load in the
144 conventional niche- the lung as well as in the liver. Mtb could be detected in the liver
145 consistently across several experiments in 4 weeks post-infection and the bacterial load
146 increased till week 10 **(Fig 2A and B).** Consistent with the Mtb burden, phalloidin and
147 hematoxylin, and eosin (H and E) staining of the infected liver at 8 weeks post-infection
148 showed localized cellular aggregation forming ectopic granulomas forming a granuloma-
149 like structure **(Fig 2C and S2C).** Further staining the liver sections with CD45.2 antibody
150 shows clustering of immune cells in Mtb infected mice liver **(Fig S2D).** To assess whether
151 liver infection leads to deranged liver function in the aerosol model, we analyzed the levels
152 of liver functional enzymes like albumin aspartate transaminase (AST), alanine
153 transaminase (ALT), and gamma-glutamyl transpeptidase (GGT) in the sera. Till week 10
154 post-infection, sera levels of these markers remain almost unchanged at the different time
155 points post-infection **(Fig S2B).** Since hepatocytes, the principal parenchymal cells of the

156 liver constitute 70-80 percent of the liver by weight, we hypothesized whether hepatocytes
157 could harbor Mtb, in the murine model of infection. To this end, we isolated primary
158 hepatocytes from the mice at different time points post-infection. The purity of the isolated
159 hepatocytes was validated by multiple methods- morphologically hepatocytes can be
160 identified by their distinct hexagonal architecture, round nucleus, some of which are
161 binucleated as observed in Alexa fluor phalloidin 488 and DAPI stained hepatocytes **(Fig**
162 **2E)**. Flow cytometry staining with antibody against hepatocyte specific marker
163 asialoglycoprotein receptor 1 (ASGR1) protein, confirmed that almost 100 perfect of the
164 isolated cells are primary hepatocytes as seen in **(Fig 2F)**. It was further validated by
165 confocal microscopy as all the cultured cells specifically stained for ASGR1 protein **(Fig**
166 **2G)**. After thorough confirmation of the identity and the purity of the hepatocytes, the cells
167 were lysed and plated. Like the whole liver CFU, Mtb infected PHCs at 4 weeks post-
168 infection with substantial bacterial load at week 6 and week 8 **(Fig 2H).** Staining with
169 antibody for Mtb-specific Ag85B protein in both the infected tissue sections and cultured
170 hepatocytes isolated from the *in vivo* infected mice revealed the presence of Mtb within
171 hepatocytes **(Fig 2D and 2I)**. Besides the aerosol route, infection intraperitoneally also
172 led to hepatocyte infection, also led to hepatocyte infection as early as day 10 **(Fig S2A).**
173 Further, to prove the spread of Mtb to the liver in other model organisms, we infected
174 guinea pigs with 200 CFU of Mtb and analyzed the bacterial load in the lung, liver, and
175 spleen at week 4 and week 8 post-infection **(Fig S3A)**. At both the time points we could
176 observe robust liver infection with granulomatous structure in the liver, proving that the
177 dissemination of Mtb to the liver occurs across multiple model animals **(Fig S3B).**

178

179 **Hepatocytes provide a replicative niche to Mtb.**

180 Consistent data from human TB patients and aerosol murine model prompted us to
181 develop an in vitro model of Mtb-hepatocyte. We examined Mtb infection in several
182 hepatocyte cell lines of mouse and human origin along with primary murine hepatocytes.
183 Infection studies with fluorescently labeled Mtb *H37Rv* were carried out with primary
184 murine hepatocyte cells (PHCs), HepG2, Huh-7, and AML-12 **(Fig 3A, B, and C).** The
185 multiplicity of infection was titrated both in PHCs and HepG2 with the MOI of 1, 2.5, 5,
186 and 10. MOI 10 consistently showed an infectivity of more than 60% in both HepG2 and
187 PHCs **(Fig S4 A, B, and C).** While we acknowledge that MOI 10 is moderately high,
188 several well-cited studies have used MOI 10 for various conventional phagocytes and
189 other non-conventional cell types like mesenchymal stem cells, adipocytes and human
190 lymphatic endothelial cells[33-37]. Hence MOI 10 was selected for further experiments
191 Macrophage cell lines RAW 264.7, THP-1, and mouse bone marrow-derived
192 macrophages (BMDMs) were used as positive controls. Even though PHCs, HepG2, Huh-
193 7, and AML-12 are not considered to be classical phagocytic cells, all cells showed
194 infectivity of more than 60 percent after 24 hours, comparable to RAW 264.7, THP-1 and
195 BMDMs **(Fig 2A, B).** Analysis of bacterial load in the PHCs post-infection showed colony-
196 forming units (CFU) like RAW 264.7, THP-1, and BMDMs, supporting microscopic
197 observations **(Fig 3C).** Mtb in macrophages is known to remodel the intracellular
198 environment to survive within phagosomes. We studied Mtb growth kinetics within
199 hepatocytes using GFP-labeled Mtb *H37Rv* in PHCs and HepG2 **(Fig 3D and F).** Mean
200 fluorescent intensity measurements showed a consistent increase in GFP intensity in both
201 PHCs and HepG2 with increasing time **(Fig 3E and G).** Fold change in replication

202 dynamics with respect to 5 HPI showed that, while bacterial growth in macrophages
203 plateaus after 48 hours post-infection, Mtb continues to grow in both HepG2 and PHCs
204 **(Fig 3H).** Our studies thus establish that hepatocytes, besides being robustly infected by
205 Mtb, also provide a favorable replicative niche for Mtb.

206 **Transcriptomics of infected hepatocytes reveal significant changes in key**
207 **metabolic pathways.**

208 To understand Mtb-induced changes in the hepatocytes and the underlying mechanisms
209 of how hepatocytes provide a favorable environment to the pathogen, we performed
210 transcriptomic analysis of the infected and sorted HepG2 cells at 0 hours (5 hours post
211 incubation) and 48 hours post-infection. Sorting before RNA isolation specifically enriches
212 the infected cellular population thus eliminating cellular RNA from uninfected cells **(Fig**
213 **4A**). Unsupervised clustering segregated the data into 4 distinct groups on the PC1 with
214 a variance of 27 percent, showing good concordance within the replicates **(Fig 4B).** The
215 close spatial clustering for the two 0-hour time points corresponding to uninfected and
216 infected is indicative of relatively less transcriptomic changes. On the other hand, the
217 spatial segregation of the 48 hours datasets suggests clear differences between the RNA
218 transcripts of uninfected and infected cells. The differentially expressed genes were
219 calculated using DE seqR with fold change >0.5 and a false discovery rate of <0.2. Gene
220 ontology (GO) enrichment analysis for the differentially regulated pathways at both the
221 early (0 hours) and the late (48 hours) infection time points is shown in **(Fig 4C).** At 0
222 hours post-infection, the immediate stress response pathway of the cell, involving ROS
223 generation, intracellular receptor signaling pathways, and response to xenobiotic stresses
224 got activated, while at a late time point, Mtb modulated some of the key immuno-metabolic

225 pathways like macroautophagy, cellular respiration, proteasomal degradation pathway,
226 response to type I interferon, IκB kinase/NF-κB signaling, etc **(Fig 4D).** Major alterations
227 in the vacuolar and vesicular transport at 48 hours are indicative of the dynamic changes
228 in the phagosome maturation pathway **(Fig 4D).** Volcano plot analysis showed greater
229 relative changes in the gene expression pattern at 48 hours compared to 0 hours, with
230 many genes like *CXCL10, CXCL11, IDO, CCL5* etc being greatly upregulated **(Fig 4E,**
231 **4F).** Interestingly, our RNA sequencing data indicated major changes in various facets of
232 lipid metabolic pathways like fatty acid biosynthesis pathway, glycerolipid and
233 glycerophospholipid metabolism, cholesterol biosynthesis pathways, etc. Several key
234 genes like *FASN, DGAT1, DGAT2*, *HMGCR*, etc. were upregulated, indicating the
235 possibility of greater synthesis of neutral lipids. Thus, transcriptomic studies shed light on
236 several of the key Mtb-induced changes in the hepatocytes.

237 To understand the difference and similarities between the pathways that get affected in
238 macrophages compared to hepatocytes during Mtb infection, we compared the gene
239 expression analysis data from Mtb-infected HepG2, 48 hours post-infection with THP-1
240 infected macrophages, 48 post-infection, taken from Kalam et al.,[35] **(Fig S5 A, B).** The
241 comparison provides insights regarding how Mtb modulates different pathways
242 depending on the type of the host cell infected. In THP-1, most of the altered pathways
243 are related to mounting an effective immune response to the bacteria like type 1 interferon
244 signalling pathway, regulation of cytokine secretion, leukocyte chemotaxis, response to
245 zinc, etc while in HepG2 the pathways that are getting altered are related to metabolism
246 like response to xenobiotic stimulus, macroautophagy, glycerophospholipid and
247 glycerolipid metabolism, and cellular respiration. This comparative analysis is indicative

248 of Mtb's ability to harness the metabolic richness of hepatocytes probably as a source for
249 nutrients. Moreover, being a non-immune cell type hepatocytes might lack a robust innate
250 immune pathway like the macrophages and hence be less likely to clear mycobacterial
251 infection.

252 **Increased fatty acid synthesis drives Mtb growth in hepatocytes.**

253 Mtb survival in foamy macrophages is driven by nutrient acquisition from the lipid
254 droplets[36]. Transcriptomic studies of Mtb-infected cells also showed upregulated
255 pathways for lipid metabolism. Examination of Lipid droplets in both PHCs and HepG2
256 revealed an increase in the number of lipid droplets at 24 hours post-infection **(Fig 5A**
257 **and B).** Time kinetic analysis of BODIPY intensity in the infected HepG2 at different days
258 post-infection indicated a concomitant increase in lipid droplets with the progress of
259 infection **(Fig 5C).** Moreover, in PHCs, GFP labeled Mtb showed a high degree of
260 colocalization with the lipid droplets **(Fig 5D).** Lipid droplets are single membrane-bound
261 depots consisting mainly of neutral lipids like diacylglycerols (DAGs), triacylglycerols
262 (TAGs), and cholesterol esters (CEs)[38].

263 Mass-spectrometric analysis of the infected and uninfected HepG2 cells at 24 hours post-
264 infection, showed an increase in both TAGs and DAGs and CEs with a decrease in the
265 levels of free cholesterols, indicating Mtb-induced changes in the neutral lipid
266 biosynthesis **(Fig 5E).** To understand whether Mtb utilizes host lipid droplets as a source
267 of nutrients in hepatocytes, we treated Mtb-infected hepatocytes with specific inhibitors
268 of de-novo fatty acid biosynthesis (C75) and TAG biosynthesis (T863) **(Fig S6 A).**
269 Interestingly, inhibiting both de-novo fatty acid biosynthesis as well as TAG biosynthesis

270 reduced the bacterial load in both PHCs and HepG2 by almost 1.0-1.5 log fold **(Fig 5G**
271 **and H)**. In THP-1 macrophage, although C75 reduced bacterial load by 0.5 log fold but
272 T863 did not affect the bacterial load **(Fig 5I).** To get better insights into the nutritional
273 dependency of intracellular Mtb on hepatocyte lipid source, we metabolically labelled
274 HepG2 with 7.5 µg/ml of fluorescently tagged fatty acid (BODIPY 558/568 C_{12}) which
275 subsequently accumulated into host lipid droplets. After 16-20 hours, the labelled cells
276 were treated with T863 and C75. Although T863 significantly reduced the load of the
277 intracellular TAGs, C75 had little effect on the level of accumulated TAGs and showed a
278 phenotype like the DMSO control **(Fig S6 C and D).** We infected these three set of cells
279 with Mtb (MOI:10) for 24 hours. The Mtb isolated from DMSO and C75 treated HepG2
280 became distinctly labelled with highly fluorescent lipid bodies, but the fluorescence signal
281 in Mtb derived from T863 treated cells was quite low and sparse **(Fig 5F and S7 A).**
282 Considering that host-derived fatty acids are converted to triacylglycerols (TAGs) in the
283 bacterial cytoplasm as a source of carbon and energy, we wanted to check whether the
284 TAG synthesis machinery was modulated in the hepatocyte-infected Mtb. To this end, we
285 isolated Mtb from HepG2, 48 hours post-infection, and analysed for key genes involved
286 in TAG biosynthesis. Mtb grown in DMEM was used as a control. Interestingly, *Tgs1,*
287 *Tgs4, Rv 1760*, etc were upregulated by 6-8-fold, indicating an active Mtb transcriptional
288 change in Mtb to utilize and store host-derived lipids **(Fig S6 B).** Cumulatively, our studies
289 thus demonstrate fatty acid biosynthesis and TAG formation to be important for Mtb
290 growth in hepatocytes.

291 To assess the status of the neutral lipids in the liver, BODIPY staining was conducted in
292 the liver cryosections of uninfected and infected mice (8 weeks post-infection). The liver

293 of Mtb-infected mice bears more lipid bodies **(Fig S8 A).** Co-immunostaining of BODIPY
294 and Ag85B also indicated a certain degree of colocalization of Mtb and Lipid bodies in the
295 liver **(Fig S8 B).** Next, we stained the liver of Mtb-infected mice at 2-, 4- and 8-weeks
296 post-infection with LipidTOX neutral red dye. Surprisingly we found an elevated signal
297 intensity of the dye at 8 weeks post-infection. This shows that in mice, Lipid droplets might
298 correlate with Mtb burden **(Fig S8 C, D).** Our data comprehensively establishes infection-
299 induced lipid droplet accumulation as a pathogenic outcome of Mtb involvement in the
300 liver during the chronic stage of infection.

301 **PPARγ upregulation in Mtb-infected hepatocytes leads to augmented lipid**
302 **biogenesis.**

303 To understand the molecular mechanism behind the accumulation of lipid droplets in the
304 Mtb-infected liver at 8 weeks post-infection, we investigated the expression patterns of
305 the transcription factors involved in the regulation of the genes of lipid biogenesis in our
306 RNA-seq data. At 48 hours post-infection, the transcript levels of Peroxisome proliferator-
307 activated receptor-gamma (PPARγ) were upregulated by 5-6-fold. To validate, that we
308 performed quantitative real-time PCR analysis of the *PPAR γ* gene in the infected HepG2
309 at 48 hours post-infection. With respect to the uninfected control, *PPAR γ* was upregulated
310 by 3-4-fold. Besides, downstream adipogenic genes that are directly or indirectly
311 controlled by *PPARγ* like *MGAT1*, *FSP27*, *FASN*, *DGAT1*, *DGAT2*, *ACAT1, ACAT2,*
312 *ADIPSIN* etc were all upregulated by more than 2-fold in the infected cells. **(Fig S9 A).**
313 Immunoblot also revealed a greater level of PPARγ protein in primary mouse hepatocytes
314 at 24 hours and 48 hours post-infection in the Mtb infected cells **(Fig 6C, D)** .In the in-vivo
315 Mtb aerosol infection model, *Pparγ* expression levels showed an intriguing trend, at week

316 2 post-infection, the expression level was comparable to the uninfected control, while at
317 week 4 post-infection, the expression level spiked to 1.5-2-fold, reaching 3-4 fold at week
318 8 **(Fig 6B).** The pattern of expression of *Pparγ* in the infected liver correlated with the
319 bacterial load in the liver, where we see the induction at week 4 when Mtb reaches the
320 liver and maximum expression at week 8 when the load of Mtb is considerably high.
321 Besides, PPARγ, some of the critical enzymes involved in fatty acid biosynthesis, TAG
322 biosynthesis, cholesterol esterification like *Fasn, Dgat1, Dgat2, Mgat1, Acat1, Acat2* etc
323 showed a temporal increase in expression levels at the later time points post-infection
324 **(Fig 6A).** We then used a specific inhibitor of PPARγ, GW9662 (20 μM) and agonist of
325 PPARγ, rosiglitazone (20μM) in infected HepG2 and quantified the bacterial load after 48
326 hours. Surprisingly, inhibition of PPARγ decreased the bacterial load by almost 2-fold,
327 while chemically inducing PPARγ increased the bacterial load considerably **(Fig 6 E and**
328 **F, and S9B)**. Moreover, LD number in cells also directly correlated with the levels of
329 PPARγ **(Fig 6G and H).** To investigate whether, PPARγ expression was also induced in
330 the liver of infected mice, we examined PPARγ in the liver post infection. Interestingly, we
331 found enhanced expression PPARγ in the liver of the mice at 8 weeks post infection **(Fig**
332 **S9 C and D).** Moreover, PPAR-γ intensity in hepatoctyte was also high in the infected
333 liver **(Fig S9 E).** Thus, PPARγ activation resulting in lipid droplets formation by Mtb might
334 be a mechanism of prolonging survival within hepatocytes.

335

336

337

338 **Hepatocyte resident Mtb displays a drug-tolerant phenotype.**

339 The success of Mtb as a pathogen is partially attributed to its ability to survive and adapt
340 to antibiotics[39]. Again Mtb-induced lipid accumulation in the liver might influence the
341 activity of the various anti-TB drugs[40]. Hepatocytes contain both phase I and phase II
342 drug metabolizing enzymes (DMEs). Further, the pharmacological potency of lipophilic
343 drugs is determined by the rate at which these drugs are metabolized to inactive
344 products[41, 42]. Cytochrome P450 monooxygenases (cyp450s) system is the key phase
345 I DMEs and known to interact with rifampicin. We therefore analysed whether Mtb
346 infection influences the cyp genes in hepatocytes. *CYP3A4* and *CYP3A43* respectively,
347 both of which metabolize anti-TB drug rifampicin were upregulated in Mtb infected HepG2
348 by approximately 4-fold and 2-fold respectively **(Fig S10A).** Moreover, *NAT2* gene
349 responsible for N-acetylation of isoniazid was also upregulated in the Mtb infected HepG2
350 by almost 2-fold) **(Figure S10 A).** We therefore argued that hepatocyte resident Mtb may
351 display higher tolerance to rifampicin. Towards this, we treated Mtb-infected HepG2 and
352 PHCs with different concentrations of Rifampicin (0.1, 0.5, 5 µg/ml) for 24 hours and CFU
353 enumerated the bacterial after lysis. RAW 264.7 was kept as macrophage control with
354 the similar experimental setup. The percentage of bacteria which survived the drugs was
355 the drug tolerant population. Both HepG2 and PHCs resident Mtb were significantly
356 tolerant to (25-30%) to rifampicin, as compared to the macrophages **(Fig 7A and B).**
357 Almost 10 percent of the bacterial population in HepG2 display a tolerogenic phenotype
358 at the highest antibiotic concentration **(Fig 7B).**

359 We also examined Mtb susceptibility to isoniazid (INH), which is predominantly
360 metabolized (50–90%) via N-acetylation of its hydrazine functionality by arylamine N-

361 acetyltransferase 2 (*NAT2*)[43]. Interestingly, KEGG analysis of transcriptomic data
362 suggested several genes in this pathway to be upregulated in hepatocytes infected with
363 Mtb **(Fig S10 B).** Experimental studies indeed showed higher tolerance of Mtb to INH in
364 both primary hepatocytes and HepG2 at different concentrations (0.1, 0.5, 5 µg/ml) **(Fig**
365 **7A and C).** Moreover, transcript levels of some of the key DMEs (were upregulated in the
366 liver of the infected mice, 8 weeks post-infection like *Nat2, Cyp2e1, Slco1b2*, *Ces1, Ces2,*
367 *and Aadac* (upregulated by almost 2-3-fold) **(Fig 7F).** To corroborate the CFU data, we
368 repeated the same experiment **(Fig 7A)** and looked at the bacterial load within each
369 PHC/BMDM using high-resolution confocal microscopy. Mouse BMDMs were as a
370 macrophage control. Here also we have calculated the % tolerance as a ratio by
371 measuring the mean fluorescent intensity of GFP-Mtb per hepatocyte treated with drug
372 to MFI of GFP-Mtb per hepatocyte treated with DMSO (control). Extensive analysis of
373 more than 200 cells showed distinctly presence of more Mtb within PHCs treated with
374 both rifampicin and isoniazid than in BMDMs treated with the same concentration of the
375 drugs **(Fig 7D, E and S11A).**

376 Drug tolerance is the phenomenon of Mtb surviving drug treatment for longer durations in
377 the absence of any resistance mechanisms. It is a bacterial property influenced by both
378 bacterial and host-induced factors[23, 44]. To check whether Mtb derived from
379 hepatocytes, post-drug exposure has altered drug sensitivity or not, we conducted a
380 resazurin microtitre assay with different dilutions of both rifampicin and isoniazid with Mtb
381 derived from PHCs treated with DMSO, Mtb derived from PHCs post-exposure to
382 rifampicin and Mtb derived from PHCs post-exposure to isoniazid. Mtb from all three
383 different setups did not show any alterations in their MIC values, displaying no change in

384 drug sensitivity (**Fig S12 A**). The increased tolerance of Mtb within the hepatocytes can
385 also be attributed to the increased activity of the drug efflux pumps. Drug efflux pumps
386 like Rv1258c, Rv1410, and Rv1819c are known to get upregulated under drug stress
387 conditions, preventing the accumulation of the drugs and thereby decreasing drug
388 sensitivity. To this end, we isolated intracellular Mtb RNA from HepG2 treated with DMSO,
389 0.5 µg/ml rifampicin, and 0.5 µg/ml isoniazid and checked for the expression of key drug
390 efflux pumps like *Rv 1258c. Rv1410, Rv1819* etc in these three Mtb populations **(Fig S12**
391 **B, C and D).** Interestingly, quantitative RT-PCR analyses of these Mtb genes did not show
392 any upregulation of these transporters in Mtb derived from HepG2 exposed to rifampicin
393 and isoniazid, indicating that drug tolerance phenotype can be better attributed to host
394 intrinsic factors rather than Mtb efflux pumps. Our data show that Mtb-infection of
395 hepatocytes induces DMEs, and this host-specific extrinsic activation may result in
396 decreased bioavailability or increased inactivation of anti-TB drugs.

397 **Discussion**

398 Over the years, various anatomical and cellular environments conducive to Mtb infection
399 have been identified, particularly concerning its latency[45, 46]. Pulmonary TB typically
400 presents with classical symptoms such as persistent coughing and mucus production due
401 to lung involvement[7]. While systemic manifestations like weight loss, fatigue, and loss
402 of appetite are commonly linked to TB progression, the underlying factors driving these
403 metabolic derangements remain unexplored. Our study sheds light on hepatocytes as a
404 previously unrecognized site for Mtb survival and replication. We have observed that Mtb
405 infection disrupts hepatocyte lipid metabolism via PPARγ, leading to increased levels of
406 fatty acids and triglycerides that the bacteria utilize for sustenance and proliferation. We

407 hypothesize that liver involvement in chronic TB, characterized by lipid imbalance, may
408 contribute to TB-associated metabolic complications. Intriguingly, a recent investigation
409 demonstrated that hepatic PPARγ activation induces the expression of growth
410 differentiation factor 15 (GDF-15), a crucial regulator of weight loss observed in ketogenic
411 diets[47].

412 In a chronic disease like tuberculosis (TB), which persists over an extended period, it is
413 quite surprising that Mtb infection of hepatocytes has been ignored thus far. While
414 previous research has explored liver infection by Bacillus Calmette-Guérin (BCG) using
415 an intra-venous model in mice, the bacilli were predominantly found within tissue-resident
416 macrophages or Kupffer cells at 15 minutes and 2 days post-infection[48]. However, our
417 study consistently identified the presence of Mtb within hepatocytes in a murine aerosol
418 infection model after the fourth week. Similarly, in a guinea pig aerosol infection model,
419 liver infection was evident, marked by distinct granulomas by week 4. Furthermore,
420 analysis of human biopsy liver samples from pulmonary TB patients revealed ectopic
421 granuloma-like structures within the liver hepatocytes, with the presence of Mtb-specific
422 Ag85B signals within hepatocytes. Together, these findings underscore hepatocytes as a
423 novel niche for Mtb persistence, shedding new light on the pathogenesis of TB.
424 Interestingly, in infected armadillos, *M. leprae* is shown to infect hepatocytes and hijack
425 liver homeostatic, regeneration pathways to promote *de novo* organogenesis[49].

426 The increased expression of PPARγ induced by Mtb in hepatocytes results in elevated
427 levels of cholesterol esters (CE 16:0, 18:0, and 18:1), diacylglycerols (DAGs 36:1, 36:2,
428 and 34:1), and triacylglycerols (TAGs 18:1/36:2, 18:0/36:2, and 18:0/36:1), leading to
429 enhanced lipid droplets. Alongside the colocalization of labeled Mtb with lipid droplets in

430 primary hepatocytes, the upregulation of key TAG biosynthesis genes such as *Tgs1*,
431 *Tgs4*, and *Rv1760* in Mtb residing within hepatocytes underscores a transcriptional
432 rewiring within the pathogen to assimilate lipids. Using PPARγ agonists and antagonists,
433 corresponding decreases or increases in bacterial burden were observed, underscoring
434 the pivotal role of PPARγ in Mtb survival within hepatocytes. The lipid remodeling induced
435 by Mtb infection in hepatocytes is recapitulated in the murine aerosol model, where an
436 increased number of lipid droplets was observed at week 8, accompanied by localized
437 accumulation of immune cells and granuloma-like structures.

438 Previous studies have demonstrated that Mtb-infected macrophage populations can
439 induce PPARγ expression through the mannose receptor-dependent pathway leading to
440 enhanced lipid biosynthesis, production of anti-inflammatory mediators, and prevention
441 of host cell apoptosis[50, 51]. Recent findings have further underscored heightened levels
442 of PPARγ in peripheral blood mononuclear cells (PBMCs) from TB patients with elevated
443 cortisol levels and increased disease severity[52]. Moreover, what distinguishes
444 hepatocytes is their pivotal role in systemic lipid metabolism by regulating de novo fatty
445 acid synthesis, TAG synthesis, fatty acid oxidation, and the regulation of LDL and
446 VLDL[22, 53]. Mtb-mediated perturbation of these vital processes can lead to a sequela
447 of metabolic disorders such as non-alcoholic fatty liver disease (NAFLD), dyslipidemia
448 and insulin resistance. Accumulation of lipids within hepatocytes offers advantageous
449 conditions for Mtb survival. In macrophages, heightened intracellular lipid levels have
450 been observed to impede autophagy and the acidification of phagolysosomes, both
451 crucial for bacterial eradication[54]. Despite these parallels, comparative transcriptomic
452 analyses of infected HepG2 cells with THP1 cells highlight differences in pathways such

453 as vacuolar and vesicular transport, xenobiotic metabolism, macroautophagy, and cellular
454 respiration. Furthermore, hepatocytes secrete hepatokines, a class of proteins serving as
455 signaling molecules, with diverse roles in metabolism, inflammation, and energy
456 homeostasis, thereby influencing the host-pathogen interplay[13].

457 Additionally, we suggest that Mtb infection of hepatocytes creates a drug-tolerant
458 environment in the liver due to activation of DMEs, many of which are earlier shown to
459 metabolize the two frontline drugs, isoniazid and rifampicin. Moreover, lipid accumulation
460 in the liver might also indirectly alter the levels of the drug metabolizing enzymes as
461 reported in previous studies[40, 55]. Upregulation of transcripts is not only observed in
462 infected cells *in vitro*, but also in the livers of mice eight weeks after Mtb infection.
463 Particularly noteworthy is the upregulation of NAT-2, which controls the rate-limiting step
464 of acetylating isoniazid into acetylisoniazid. This metabolite is further processed into
465 acetylhydrazine and isonicotinic acid, ultimately reducing the drug's effectiveness against
466 Mtb. Similarly, key rifampicin-metabolizing esterase genes such as Ces1, Ces2, Aadac,
467 and transporter Slco1b2 exhibit upregulation, potentially influencing the drug's distribution
468 and metabolism in the body. The activation of DMEs can significantly modify the
469 pharmacokinetics and pharmacodynamics of anti-TB medications, resulting in suboptimal
470 drug concentrations and the emergence of drug-resistant strains[56].

471 Although animal models offer valuable insights into Mtb infection and TB pathology, they
472 fall short of fully replicating the complexities of human TB. Several recent studies in
473 COVID-19 patients have shown that hepatocytes get infected with SARs-CoV-2, thereby
474 increasing gluconeogenesis and hyperglycemia [57, 58].) With compelling reports
475 associating hepatic steatosis with the onset of type 2 diabetes mellitus (T2DM), we

476 speculate that TB-induced perturbations in lipid metabolism might predispose chronic TB
477 patients to T2DM and vice versa[59, 60]. Through our investigation, we propose that
478 future studies in human TB patients might scrutinize this metabolically rich hepatocyte
479 niche to understand multiple organ-wide derangements in TB pathogenesis.

480 **Materials and Methods**

481 **Ethical clearances**

482 **Human studies:**

483 Paraffinized non-Mtb infected, and Mtb-infected human autopsied liver specimens were
484 obtained from the Postgraduate Institute of Medical Education and Research,
485 Chandigarh, India. The Institutional Ethics Committee of CSIR-IMTech (Council of
486 Scientific and Industrial Research-Institute of Microbial Technology) approved all research
487 experiments involving human samples (Approval no [IEC (May 2021) #6]). The samples
488 utilized in the study are from a library of autopsied human specimens in PGIMER
489 (Postgraduate Institute of Medical Education and Research). The consent is provided by
490 the relatives of the deceased person while its submission to the PGIMER.

491 **Animal studies:**

492 All the mice (C57BL/6) were housed in the animal house at the National Institute of
493 Immunology (NII) before being transported to the TACF-ICGEB (Tuberculosis Aerosol
494 Challenge Facility), for subsequent animal infection studies. The animal experiments
495 were performed adhering to the institutional guidelines (Approval number: Institutional
496 Animal Ethical Committee, IAEC 543/20.). Female Hartley Dunkan guinea pigs were used

497 for infection studies in TACF-ICGEB in accordance with the institutional guidelines
498 (Approval number: Institutional Animal Ethical Committee, IEAC #440/17)

499 **Confocal microscopy and Immunofluorescence measurements:**

500 Lipid droplets were stained by BODIPY 493/503 dye. Primary mouse hepatocytes and
501 HepG2 cells were grown on 12 mm coverslips at respective densities as per the
502 experimental requirement. Cells were washed with 1X PBS (HiMedia M1452-500G), fixed
503 by 4% paraformaldehyde, and incubated at room temperature for 15 minutes. After
504 incubation, the cells were washed thrice with 1X PBS followed by staining with 10 μM
505 BODIPY dye in 1XPBS for 45 minutes at room temperature. After the staining, the excess
506 dye was removed by washing thrice with 1X PBS. To check for the acidified compartments
507 within the cells, LysoTracker Red DND-99 (L7528) was added to the cells at a
508 concentration of 500 nM for 30 minutes at 37° Celsius, followed by washing thrice with
509 1X PBS to remove the residual dye. The cells were fixed with 4% paraformaldehyde as
510 previously mentioned. For staining with various antibodies, the cells were permeabilized
511 with 0.2% Triton-x 100 (X-100-1L) for 15 minutes, followed by proper washing with 1X
512 PBS. The cells were then blocked by 2% BSA in 1X PBST for 1 hour at room temperature.
513 Post blocking, the cells were treated with primary antibody overnight at 4°Celsius,
514 followed by proper washing with 1X PBS. Secondary antibody (1:500 dilution) was added
515 to the cells for 1 hour at room temperature. Three washes with 1X PBS were given. The
516 nucleus was stained with DAPI (Sigma D9542-5MG) at 1ug/ml concentration for 20
517 minutes at room temperature. The excess DAPI was washed with 1X PBS followed by
518 mounting with ProLong Gold Antifade mountant (P36930). Images were acquired by Zeiss
519 LSM 980 Laser scanning confocal microscope.

520 **Image Analysis:**

521 Analysis was done using Image J and Zen blue software. Mean fluorescent intensity/ cell
522 was calculated by corrected total cell fluorescence (CTCF) = Integrated Density – (Area
523 of Selected Cell x Mean Fluorescence of Background readings). Signal intensity in tissue
524 sections were normalized to respective areas. For colocalization of Mtb with various intra-
525 cellular markers, each data point represents a single field with 6-8 infected cells. More
526 than 100 cells across 4 independent experiments were analyzed. Serial confocal sections
527 were acquired with Z-stacks spanning 10-15 uM. The percentage of Mtb in the respective
528 markers were calculated by calculating the Mtb voxels colocalizing in the respective
529 markers. The image was analyzed by Zen Blue software (Zeiss) and Image J.

530 For percentage tolerance of Mtb within hepatocytes, we have calculated the ratio by
531 measuring the mean fluorescent intensity of GFP-Mtb per hepatocyte treated with drug
532 to MFI of GFP-Mtb per hepatocyte treated with DMSO (control). BMDMs were used as
533 the macrophage control. More than 20 fields, each consisting of more than 4 infected
534 cells have been used for analysis. MFI/ cell was calculated using the Zeiss ZEN blue
535 image analysis software.

536 **Tissue Immunofluorescence staining:**

537 **Paraffin sections**

538 Five-micron thick sections of paraffin-embedded tissue sections were taken in poly-L-
539 Lysine coated slides (P0425-72EA). Deparaffinization was performed by heating the
540 slides at 50°C for 20 seconds (3 times) till the wax melts, followed by the subsequent
541 steps, 100% xylene (Merck, CAS-1330-20-7) for 10 minutes (3 times), xylene and

542 absolute ethanol (Merck, CAS- 64-17-5) for 10 minutes, 100% ethanol for 10 minutes,
543 70% percent ethanol for 5 minutes (2 times), 50% ethanol, distilled water for 5 minutes
544 (2minutes) and a final wash in 1x PBS for 5 minutes (2 times). Antigen retrieval was
545 performed in an antigen retrieval buffer (10mM Sodium Citrate, 0.05% tween-20, pH: 6)
546 by heating the slides at 60°C for 15 minutes. After antigen retrieval, permeabilization was
547 performed with 0.4% Triton-X 100 in 1X PBS for 20 minutes followed by proper washing
548 with 1x PBS. Blocking was done with 5% BSA for 1 hour. Sequential addition of primary
549 antibody was performed at 1:100 dilution at 4°C overnight. Primary antibody was washed
550 with 1X PBS followed by counter stain with DAPI nuclear stain at 1 ug/ml concentration.
551 Mounting was done with a drop of vectashield (sigma-aldrich, F6182-20ml). The slides
552 were visualised in Zeis LSM 980 confocal microscopy at 40X (oil) magnification.

553 **Cryosections**

554 Seven-micron thick cryosections were taken in poly-L-Lysine coated slides (P0425-
555 72EA). The sections were washed with 1X PBS, 3 times for 5 mins each. Permeabilisation
556 was done with 0.25% Triton-X 100 in 1X PBS for 15 minutes followed by washing with 1X
557 PBS. Blocking was done with 5% BSA for 1 hour followed by incubation with primary
558 antibody overnight at 4°C. After that the slides were washed with 1X PBS 2 times for 5
559 minutes each followed by incubation with fluorophore conjugated secondary antibody for
560 45 minutes. The slides were washed with 1X PBS followed by counterstain with DAPI at
561 1ug/ml concentration. Mounting was done with a drop of Vectashield (Sigma-Aldrich,
562 F6182-20ml). The dilution of the dyes and antibodies used in the staining are mentioned
563 in the table.

564 For staining with BODIPY, the sections were incubated with 15 ums of BODIPY for 40
565 minutes at room temperature. The slides were visualized in Zeis LSM 980 confocal
566 microscopy at 40X (oil) magnification.

567 **Fluorescence in-situ hybridization:**

568 FISH was used to detect Mtb in infected human liver following published protocols (1-3).
569 Briefly, the paraffinized human liver tissue sections were initially deparaffinized using a
570 serial washing step with xylene and ethanol, following which the sections were treated
571 with 1 mg/ml Proteinase K and 10 mg/ml Lysozyme in 10 mM Tris (pH 7.5) at 37°C for 30
572 min. Next, the samples were incubated in the Prehybridization buffer at 37°C for 1 h.
573 Prehybridization buffer is composed of 20% 2X Saline sodium citrate (SSC), 20% Dextran
574 sulfate, 30% Formamide, 1% 50X Denhardt's reagent, 2.5% of 10 mg/ml PolyA, 2.5% of
575 10 mg/ml salmon sperm DNA, 2.5% of 10 mg/ml tRNA. The slides were thoroughly
576 washed with a 2X SSC buffer. The sections were then incubated in hybridization buffer at
577 95°C for 10 min and then chilled on ice for 10 min. Further hybridization was allowed at
578 37°C overnight. Hybridization buffer is composed of prehybridization buffer plus 16S Mtb-
579 H_{37} Rv probe (5′ FITC – CCACACCGCTAAAG – 3′), which is specific for the 16S rRNA
580 of Mtb at a final concentration of 1 ng/µl. The liver tissue sections were next subjected to
581 a series of washing steps with 1X SSC at room temperature for 1 min, 1X SSC at 55°C
582 for 15 min, 1X SSC at 55°C for 15 min, 0.5X SSC at 55°C for 15 min, 0.5X SSC at 55°C
583 for 15 min, 0.5X SSC at room temperature for 10 min. Coverslips were mounted on glass
584 slides and visualized using Nikon A1R confocal microscope with a 488 nm laser.

585

586 **Acid Fast Staining and Auramine O and Rhodamine B staining in liver sections.**

587 Acid-fast staining was performed using a ZN Acid Fast Stains-Kit (K005L-1KT, HIMEDIA).
588 Prior to staining, the paraffinized samples were deparaffinized using a serial washing step
589 with xylene and ethanol 1. 100% Xylene for 6 min, 2. Xylene: Ethanol 1:1 for 3 min, 3.
590 100% Ethanol for 3 min, 4. 95% Ethanol for 3 min, 5. 70% Ethanol for 3 min, 6. 50%
591 Ethanol for 3 min, 7. Distilled water. The glass slides were flooded with Carbol Fuchsin
592 stain and heated to steam for 5 min with a low flame. The glass slides were allowed to
593 stand for 5 min without further heating. The glass slides were then washed in running tap
594 water. The glass slides were decolorized with acid-fast decolourizer for 2 min. 5. Washed
595 with tap water. 6. Counterstain for 30 sec with Methylene Blue Washed with tap water,
596 dried in air, and examined under 100x objective with oil immersion. The presence or
597 absence of bacteria in infected and uninfected samples was checked through staining
598 with Phenolic Auramine O-Rhodamine B dye (4) (1/3 dilution of stock solution) (Auramine
599 O-861020-25gm, Sigma) (Rhodamine B-R6626-100gm, Sigma). Coverslips were
600 mounted on glass slides and visualized using CLSM with a 488 nm laser.

601 **Bacterial cultures and in-vitro experiments:**

602 Virulent laboratory strains of H37Rv, BCG, and GFP-H37Rv bacterial cultures were
603 cultivated on 7H9 medium (BD Difco) supplemented with 10% Oleic Acid-Albumin-
604 Dextrose-Catalase (OADC, BD, Difco),0.05% glycerol and 0.05% tween 80 under shaking
605 at 37°C conditions for in vitro assays. The cultures were then incubated in an orbital
606 shaker at 100 rpm and 37 °C until the mid-log phase. pMN437-GFPm2 vector (Addgene,
607 32362) was used to electroporate the virulent H37Rv strain to create GFP-H37Rv, which

608 was then maintained in 50 µg/ml hygromycin 7H9-OADC medium. pMSP12: mCherry
609 plasmid (Addgene No. 30169) was electroporated in H37RV to generate Mtb-H37Rv-
610 mCherry.To prepare the single-cell suspension needed for infection tests, bacterial
611 cultures were passed through a sequence of different gauge needles five times through
612 23-gauge, 26-gauge, and three times through 30-gauge.

613 Human monocytic cell line THP-1 were obtained from American Type Culture Collection
614 (ATCC) and cultured in RPMI-1640 medium with 10% FBS at 37 °C and 5% CO2
615 incubator. THP-1 derived macrophages were obtained by incubating THP-1 cells with 20
616 ng/ml phorbol 12-myristate 13-acetate (PMA, sigma) for 24 hours followed by washing
617 and maintenance in complete media. The cells were kept in non-PMA containing
618 complete media for 16-20 hours before infection with Mtb. HepG2, Huh-7, RAW 264.7
619 and PHCS were grown in DMEM under with 10% FBS at 37 °C and 5% CO2 incubator.

620 AML-12 cells were cultured in DMEM media containing 1X insulin-transferrin-selenium
621 supplement (ITS-G), under the above-mentioned conditions.

622 In-vitro and ex-vivo infection experiments in primary cells and different cell lines were
623 performed at a Multiplicity of infection of 10 (MOI: 10) for both CFU enumeration and
624 confocal microscopy. The macrophage experiments involving THP-1 and RAW 264.7
625 involved incubating the cells with Mtb-H37Rv for 5-6 hours followed by washing with 1X
626 PBS and amikacin treatment (200 ug/ ml for 2 hours) to remove the extracellular bacteria.
627 The cells were kept for the designated time points for 24 hours, 48 hours and so on and
628 then lysed with lysis buffer (0.05 % SDS in 1X PBS) followed by plating in 7H11 plates.

629 For primary mouse hepatocytes and AML-12 cells, the cells were infected with the Mtb at
630 a multiplicity of 10 for 8 hours followed by amikacin treatment (200 ug/ ml for 2 hours).
631 For HepG2 and Huh-7, the time of incubation was 5- 6 hours followed by washing with
632 1X PBS and amikacin treatment as previously mentioned to remove the extracellular
633 bacteria.

634 The percent drug tolerant population was calculated using the following formula (A/B X
635 100) where A is the CFU in the drug treated group, B is the CFU in the untreated group.
636 The cells were morphologically checked for signs of cell death before proceeding with the
637 plating. For the inhibitor and inducer experiments, the cells were treated with the
638 respective drugs for 48 hours post uptake of Mtb. After that they were lysed and Mtb CFU
639 was enumerated.

640 **Standardization of Multiplicity of infection (MOI) for PHCs and HepG2:**

641 To standardise the MOI, HepG2 and BMDMs were infected with the following MOI of GFP-
642 Mtb as per the standardized protocol: 1, 2.5, 5 and 10. 6 hours post-infection, the cells
643 were trypsinised and fixed with 2% PFA. The percentage uptake was calculated by flow
644 cytometry. For, PHCs, the cells were infected at the above-mentioned MOI and
645 percentage infection was calculated by microscopy as (# of cells with GFP-Mtb/Total # of
646 cells *100)

647 **C57BL/6 aerosol challenge:**

648 The mice infection experiments were conducted in the Tuberculosis Aerosol Challenge
649 Facility (TACF, ICGEB, New Delhi, India). C57BL/6 mice were placed in individual
650 ventilated cages within the enclosure, maintaining a temperature of 20-25°C, 30-60 %

651 humidity and 12h-12h of light-dark cycle. Following the standardized protocol, mice were
652 infected with 200 CFUs of H37Rv in a Wisconsin-Madison chamber. To ensure proper
653 establishment of infection, two animals were euthanized 24 hours post aerosol challenge.
654 The lungs were harvested and homogenised in 1X PBS and plated in Middlebrook 7H11
655 agar plates (Difco) supplemented with 10% OADC and 0.5% glycerol. CFU enumeration
656 was done three weeks post plating.

657 **C57BL/6 peritoneal infection:**

658 The mice were injected with 10^6 CFUs of H37Rv in 0.2 ml of 1X PBS. Following infection,
659 on different days post infection, the lung, spleen, and the liver was harvested and
660 homogenized and plated in Middlebrook 7H11 agar plates (Difco) supplemented with 10%
661 OADC and 0.5% glycerol. CFU enumeration was done three weeks post plating.

662 **List of antibodies and dyes used in the study:**

Serial number	**Antibodies and dyes**	**Catalogue number**	**Company**	**Application and dilution**
1.	Rab5	2143T	CST	IF/ICC (1:200)
2.	Rab7	D9F2	CST	IF/ICC (1:200)
3.	Cathepsin D	Ab75852	Abcam	IF/ICC (1:150)
4.	LAMP1	9091T	CST	IF/ICC (1:200)
5.	EEA1	3288T	CST	IF/ICC (1:200)

6.	ASPGR1	PA5-32030	Invitrogen	IF/ICC (1:500)
7.	PPAR γ	PA3-831A	Invitrogen	IF/ICC (1:150) WB (1:1000)
5.	Ag85B	Ab43019	Abcam	IF/ICC (1:800)
6	CD45-APC (clone 104)	558702	BD biosciences	1:300
7.	β-actin rabbit polyclonal Antibody.	4967	CST	IF/ICC (1:100) WB (1:2000)
8.	Goat anti-rabbit IgG (H+L) secondary Ab Alexa fluor 555 Plus	A32732	Thermo fischer Scientific	IF/ICC (1:400)
9.	Goat anti-rabbit IgG (H+L) Secondary Antibody, Alexa Fluor 488	A11008	Thermo fischer Scientific	IF/ICC (1:400)
10.	Goat anti-rabbit IgG (H+L) Secondary Antibody, Alexa Fluor 405	A-31556	Thermo fischer Scientific	IF/ICC (1:400)

11.	Lysotracker Red	L7528	Invitrogen	500 nM
12.	BODIPY-493/503	D3922	Invitrogen	Staining (10-15 µM)
13.	BODIPY 558/568 C12	D3835	Invitrogen	Metabolic Labelling (7.5 µg/ml)
14.	Phalloidin-Alexa fluor 488	A12379	Invitrogen	IF/ICC 1 unit/slide
15.	Phalloidin-Alexa Fluor 555 plus	A30106	Invitrogen	IF/ICC 1 unit/slide
16.	HCS LipidTOX Red Neutral Lipid Stain	H34476	Invitrogen	IF/ICC (1:400)
17.	DAPI	D9542	Sigma-aldrich	1 ug/ml
18.	ZN Acid Fast Stains	K005L-1KT	Himedia	
19.	Auramine O	861020-25gm	Sigma-Aldrich	

19	Rhodamine B	R6626-100gm	Sigma-Aldrich	

663

664

665 **List of reagents in the study:**

Serial no	Reagents	Catalogue number
1.	C75	C5490-5MG, Sigma-Aldrich
2.	OA-BSA	O3008-5ML, Sigma-Aldrich
5.	GW9662	M6191-25MG, Sigma-Aldrich
6.	Rosiglitazone	R2408-10MG, Sigma-Aldrich
7.	T863	SML0539-5MG, Sigma-Aldrich
8.	Rifampicin	557303-1G, Merck
9.	Isoniazid	I3377-5G, Merck
10.	PMA (Phorbol 12-myristate 13-acetate)	P8139-1MG, Merck
11.	Mouse MCSF (macrophage colony stimulating factor)	130-101-706 (25 µg), Miltenyi Biotec

12.	Insulin-Transferrin-Selenium (ITS - G) (100X)	41400045, Gibco

666

667 **Sorting of labelled H37Rv cells**

668 The infected hepatocytes were trypsined and washed with 1X PBS followed by passing
669 through 40µm cell strainer to make single cell suspension. After that the cells positive for
670 mCherry signals were sorted using the BD FACS Aria at TACF, ICGEB. Approximately 1
671 million cells were used for RNA isolation per sample.

672 **Primary hepatocyte Isolation:**

673 After euthanizing the mice, the peritoneal cavity was opened, and the liver was perfused
674 with 1X HBSS solution till exsanguination was complete. After that collagenase solution
675 (17 mg in 30 ml of 1X HBSS) was passed for digestion. The liver was cut into small pieces
676 and kept in 25 ml of DMEM media followed by lysing the tissues with a glass pestle and
677 sieve. The cells were then passed through a 70 µM cell strainer. 25 ml of Percoll was
678 added to the cells with proper mixing. It was centrifuged at 1000 rpm for 5 minutes. The
679 floating cells were removed, and a brownish layer of pure hepatocytes pelted at the
680 bottom. The cells were counted and plated according to the experimental need on a
681 collagen coated plate.

682 **Isolation of Bone marrow derived macrophages (BMDMs) from mouse:** BMDMs
683 used for Mtb infection studies were isolated following the published protocol with minor

684 modifications[61]. Briefly, the epiphysis of the femurs and tibia from C57BL/6 mice were
685 cut and the bone marrow were gently flushed into BMDM supplemented with 10% FBS
686 and 1% penicillin streptomycin. The bone marrow cells were centrifuged at 200 X g for 5
687 minutes at 4° C. The cell pellet was aspirated with 1X PBS and treated with RBC Lysis
688 buffer (for 3 minutes on ice, followed by the addition of complete media. The cells were
689 resuspended in 5 ml of the media and passed through a 70 µm cell strainer. The cells
690 were seeded in complete DMEM supplemented with 10ng/ml of MCSF. On the third day,
691 half of the media volume was replaced by fresh DMEM supplemented with 10ng/ml of
692 MCSF. On the 7th day, the cells were trypsinised, counted and seeded according to
693 experimental requirements.

694 **Lipid Extraction protocol and Mass spectrometry:**

695 5 million HepG2 cells were infected with Mtb-H37Rv at MOI 10 and kept for 24 hours and
696 48 hours post-infection. An equal number of uninfected cells were taken. The cells were
697 scrapped, and the procedure of Bligh and Dyer was followed[62]. In brief, the cells were
698 lysed in 1% Triton X-100 after being rinsed twice with 1X PBS. Following lysis, the lysate
699 was vortexed and four volumes of methanol-chloroform (2:1) were added. After that, one
700 volume each of water, chloroform, and 50 mM citric acid was added and vortexed.
701 Following a 10-minute centrifugation at 10,000 rpm at 4° Celsius, the lower organic phase
702 was collected and dried using liquid nitrogen. All semi-quantitative lipid measurements
703 were done using previously reported high-resolution MS/MS methods and
704 chromatographic techniques on an Agilent 6545 QTOF instrument. All sterols were
705 resolved using a Gemini 5U C-18 column (Phenomenex) while DAGs/TAGs were
706 resolved using a Luna 5U C-5 column (Phenomenex) using established solvent systems.

707 **Cell lysate preparation and Western blotting:**

708 The cells were washed twice with 1X PBS followed by lysis with SDS-RIPA buffer (50 mM
709 Tris-HCl pH 7.5, 150 mM NaCl, 1 mM EDTA, 0.1% SDS, 1% Triton-X 100, 1 mM DTT, 1X
710 Proteinase inhibitor). The cells were incubated with the buffer for 30 minutes in ice
711 followed by vortexing for 5 minutes. The supernantant fraction was collected by
712 centrifuging at 10000 rpm for 20 minutes at 4°C. The protein concentration was
713 determined by bicinchoninic acid (BCA) protein estimation kit (Thermo Fisher Scientific,
714 Waltham, Massachusetts, USA, 23227) following the manufacturer's protocol. 60-80 ug
715 of protein was resolved in SDS-PAGE followed by transferring onto a PVDF membrane.
716 Blocking was done in 5% skimmed milk in 1X TBST followed by incubation with primary
717 antibodies overnight at 4°C. The membranes were washed 3 times with 1x TBST for 10
718 minutes each followed by incubation with the HRP-conjugated secondary antibody for 1
719 hour. Immobilon HRP substrate was used to develop the blots and ImageQuant
720 Chemiluminescent imaging system (LAS 500) was used to acquire the images. Band
721 intensities were measured by using ImageJ.

722 **MIC determination of Mtb isolated from primary hepatocytes and primary**
723 **hepatocytes treated with Rifampicin and isoniazid:**

724 Mtb was isolated from primary hepatocytes, primary hepatocytes treated with 0.5µg/ml of
725 rifampicin and primary hepatocytes treated with 0.5µg/ml of isoniazid. These bacteria
726 were grown to a logarithmic phase of OD_{600}= 0.6 in Middlebrook 7H9 broth supplemented
727 with 10% OADC, 0.05% glycerol and 0.05% tween 80 under shaking conditions. Single-
728 cell suspension of the Mtb was made as previously described. Two-fold serial dilutions of

729 both rifampicin and isoniazid was prepared in 0.1 ml 7H9-OADC (without Tween 80) (The
730 concentration and the dilution of the drugs have been mentioned in the figure) in 96-well
731 flat bottom microplates. Approximately $5X10^4$ Mtb cells were added to each well in a
732 volume of 0.1 ml. Control wells containing (Mtb only, medium+ inhibitor and only medium)
733 were included in the plate setup. The plate was incubated at 37°C 5 days, followed by the
734 addition of 20 µl of 0.02% resazurin for 24 hours. Visually, minimum inhibitory
735 concentration (MIC) was noted as the lowest drug concentration that prevented the
736 change of colour from blue to pink.

737 **qRT-PCR of intracellular Mtb isolated from hepatocytes:**

738 HepG2 cells were infected with Mtb at a MOI of 10 and at the respective time points post-
739 infection, the intracellular Mtb was isolated. In all experiments, the cells were treated with
740 amikacin to remove the extracellular bacteria, followed by subsequent washing by 1X
741 PBS. 4M Guanidine isocyanate was added to the flasks in equal amount to the media
742 and the cells were scrapped. The suspension was centrifuged at 3500 rpm for 7 minutes
743 and the pellet was resuspended in 350 µl of the RNA Lysis buffer of MN Kit (740955.250),
744 followed by beat beating. RNA was isolated as per the manufacturer's protocol. Isolated
745 RNA was treated with Dnase (PGM052, Puregene) for 1 hour to remove genomic DNA
746 contamination. RNA integrity was checked by running it on a 2% agarose gel with RNA
747 loading dye.

748 1 µg of RNA was reverse transcribed to cDNA using the Takara cDNA synthesis kit
749 (6110A) as per the manufacturer's protocol. Gene expression analysis by quantitative
750 real-time PCR was performed PowerUp SYBR Green PCR (Thermo fischer scientific,

751 (A25742) master mix in ABI 7500 FAST instrument. 16S rRNA was used as the
752 normalizing control and comparative Ct method was used for quantification.

753 **Fluorescent fatty acid labelling of HepG2 and isolation:**

754 HepG2 cells were incubated with 7.5 µg/ml of fluorescently tagged fatty acid (BODIPY
755 558/568 C_{12}) for 24 hours. The unincorporated fatty acids were removed by washing it
756 with 1X PBS, three times. After that the cells were treated with DMSO or inhibitors (T863
757 and C75) for 24 hours, followed by infection with Mtb at a MOI of 10, following the
758 standardized protocol of infection. A separate set of cells before infection were analysed
759 for the effect of the inhibitors on LD formation by microscopy.

760 After, 48 hours post infection, the cells were washed with 1X PBS and treated with Triton
761 X -100 (0.05% v/v in water), probe sonicated, and Mtb from the cells were isolated by
762 centrifuging at 3500 RPM for 8 minutes. Isolated Mtb cells were washed with 1X PBS and
763 fixed with 4% PFA and stained with DAPI (1mg/ml). The cells were mounted on poly-L-
764 lysine coated slides with antifade agent. The cells were visualised in Zeiss 980 LSM
765 confocal microscope at 100X, magnification.

766 **Gene expression studies**

767 **RNA isolation**

768 Total RNA was isolated from HepG2, PHCs and liver sections using the MN-NucleoSpin
769 RNA isolation kit (740955.250) following the manufacturer's protocol. For RNA
770 sequencing, an equal number of cells was used during isolation. For Liver tissue,
771 approximately 10mg was tissue was used. The quality of the RNA was verified by running

772 it on a 1.5% agarose gel and by monitoring 260/280 ratios. All the RNA samples were
773 frozen together in -80°C. For RNA sequencing, 3-5 ug of RNA was shipped in sodium
774 acetate buffer (3 M Sodium acetate, pH 5.2) with 100% Ethanol. 4 biological replicates
775 from each time point were sent for sequencing. The RNA samples with RNA integrity
776 number (RIN > 8.5) were used for library preparation.

777

778 RNA samples (for four biological replicates) were subjected to pair-end RNA sequencing
779 after rRNA depletion on the Illumina platform Novaseq-6000 at CCMB, Hyderabad, India.
780 Quality control and sequence trimming was performed using fastp (v0.23.2). The trimmed
781 paired-end reads were aligned to the human genome (GRCh38) using the HISAT2
782 (v2.2.1) pipeline. Reads were assembled into transcripts using StringTie (v2.2.1).
783 Annotation was conducted using aligned sequences and a GTF annotation file. The
784 mapped reads were then used for generating the count table using StringTie
785 (v2.2.1), genes lacking an Ensembl ID annotation were excluded. We arrived at a list of
786 62694 genes which were used for further analysis **(available through GEO accession-**
787 **GSE256184).** The differential count was performed by DEseq2 (R package) using the
788 uninfected samples of respective time points. Pathway enrichment was performed using
789 the GO database and clusters were visualized using the R package ClusterProfiler.
790 Further pathways of interest were analysed by GAGE and visualized using Pathview in
791 KEGG view.

792

793

794 **cDNA synthesis and RT-qPCR**

795 1ug of RNA was reverse transcribed to cDNA using the Takara cDNA synthesis kit (6110A)
796 as per the manufacturer's protocol. Gene expression analysis by quantitative real-time
797 PCR was performed PowerUp SYBR Green PCR (Thermo fischer scientific, (A25742)
798 master mix in ABI 7500 FAST instrument. Beta-actin was used as the normalizing control
799 and comparative Ct method was used for quantification.

800 **List of primers used in the study.**

GENE NAMES	FORWARD PRIMER (5'---------->3')	REVERSE PRIMER (5'---------->3')	
β-actin	ATGGAGGGGAATACAGCCC	TTCTTTGCAGCTCCTTCGTT	Mouse
ppar-γ	CTCTGGGAGATTCTCCTGTTGA	GGTGGGCCAGAATGGCATCT	Mouse
ppar-α	AGAGCCCCATCTGTCCTCTC	ACTGGTAGTCTGCAAAACCAAA	Mouse
fasn	CTGCGTGGCTATGATTATGG	AGGTTGCTGTCGTCTGTAGT	Mouse
acat1	CAGGAAGTAAGATGCCTGGAAC	TTCACCCCCTTGGATGACATT	Mouse
acat2	CCCGTGGTCATCGTCTCAG	GGACAGGGCACCATTGAAGG	Mouse
dgat1	TGCCCTGACAGAGCAGATGG	CAGGTTGACATCCCGGTAGG	Mouse
dgat2	TGGCGCTACTTCCGAGACTAC	TGCTGACTTCAGTAGCCTCTGTG	Mouse
nat2	ACACTCCAGCCAATAAGTACAGC	GGTAGGAACGTCCAAACCCA	Mouse
Slco1b2	GGGAACATGCTTCGTGGGATA	GGAGTTATGCGGACACTTCTC	Mouse
aadac	TACCGCTTCCAGATGCTATTGA	ACTGATTCCCAAAAGTTCACCAA	Mouse
cyp2e1	CATCACCGTTGCCTTGCTTG	GGGGCAGGTTCCAACTTCT	Mouse
ces1c	GCACTACGCTGGGTCCAAGAT	AAAGATGGTCACGGAATCCG	Mouse
ces2c	GCTGAATGCTGGGTTCTTCG	GCTGCCTTGGATCTGTCCTGT	Mouse
β-actin	AAGGCCAACCGCGAGAAGAT	GCCAGAGGCGTACAGGGATA	Human

pparγ	GGTGAAACTCTGGGAGATTCT	CTCTGTGTCAACCATGGTCA	Human
fasn	AGTACACACCCAAGGCCAAG	GTGGATGATGCTGATGATGG	Human
acat1	TACCAGAAGTAAAGCAGCATGG	TCATTCAGTGTACTGGCATTGG	Human
acat2	CTTTAGCACGGATAGTTTCCTGG	GCTGCAAAGGCTTCATTGATTTC	Human
dgat1	CAATCTGACCTACCGCGATCT	TCGATGATGCGTGAGTAGTCC	Human
dgat2	GAATGGGAGTGGCAATGCTAT	CCTCGAAGATCACCTGCTTGT	Human
nat2	CCAGAAGGGGTTTACTGTTTGG	CAGGTTTGGGCACGAGATTTC	Human
mgat1	CGCAAGTTCCAGGGCTACTAC	CTTCAGCAGCGGATAGGTGG	Human
fsp27	ATGGACTACGCCATGAAGTCT	CGGTGCTAACACGACAGGG	Human
Rv1258c	CTACGAGGCGATCCTCAACC	CGAGGATGGACAACCCGAAT	Mtb
Rv1819c	ATCGGGGTTTTCAGCGTGAT	GTCGAGCCAGTCTTGTGTGA	Mtb
Rv1218c	ATCGAGATTCGCGGACTGAC	ACATCGCCTGGAACATAGGC	Mtb
Rv1410c	ATGGTGACGCTGGTTGATGT	CGGTAGGGCGATAAGGAACC	Mtb
tgs1 (Rv3130c)	CCTTCTTATCGTCGCTCGCT	GCCAAGATCGAAGTCGGGAT	Mtb
tgs4 (Rv3088)	ACGGTCTCGTTCCTCAACAC	CCGGTGAATCGGAGAGGAAG	Mtb
lipY (Rv3097c)	TCTGCGCTCGAAACTCACTT	GCTCATCCCGTCATAGGTGG	Mtb
acrA1 (Rv3391)	ATGGCGGTCAACTACTTCGG	CCTTGGTGGGCAGATACGAG	Mtb

801

802

803

804

805

806

807 **List of reagents in the study**

Reagent	Company	Catalogue number
Immobilon Forte Western HRP substrate	Millipore	WBLUF0500
Amersham Hybond Western blotting membranes, PVDF	Merck	GE10600023
PowerUP SYBR	Thermo Fischer Scientific	A25742
Vectashield	Sigma-Aldrich	F6182
Primescript 1st strand cDNA synthesis kit	Takara Bio	6110A
NucleoSpin RNA isolation Kit	Macherey-Nagel	74106
ProLong Gold antifade reagent	Thermo Fischer Scientific	P36930
PolyFreeze Tissue Freezing medium	Sigma- Aldrich	SHH0026

Microscope slides	Himedia	BG005
Poly-Prep slides	Sigma- Aldrich	P0425-72EA
2X RNA loading dye	Thermo Scientific	R0641

808 **Softwares**

809 All the graphs have been generated using GraphPad Prism 10 and Microsoft Excel. The
810 schematics have been drawn with the help of Biorender.com.

811 **Acknowledgements**

812 We thank Dr. Lakshyaveer Singh, Tuberculosis Aerosol Challenge Facility (TACF), ICGEB
813 for mice experiments. We thank Dr. Neerja Wadhwa for helping in the NII Central Confocal
814 facility, Mr. Birendra Nath Roy for the preparation of the Cryosections, and the NII animal
815 facility for providing us with the animals. We thank the Next Generation Sequencing
816 (NGS) facility at CSIR-CCMB for transcriptomic support.

817 **Author Contribution**

818 BS and RSG conceptualized the study and analysed the data. BS, DSG, JS, MY, PS,
819 RDS performed the experiments. Human liver sections were stained by SS under the
820 guidance from AK. Transcriptomic analysis was done by JS. Sorting was done by PS and
821 RDS under the guidance from DK. Mass spectrometry analysis was conducted by AC
822 under the supervision of SSK.KM conducted the guinea pig infection experiments. BS
823 and RSG wrote the manuscript. BS, DM, DSG, AK, SSK, DK and RSG reviewed and
824 edited the manuscript. RSG supervised the project.

825 **Declaration of Interests:** The authors declare no conflicts of interests.

826 ## References

827 1. *Global Tuberculosis Report* 2023, World Health Organisation (WHO).
828 2. Seung, K.J., S. Keshavjee, and M.L. Rich, *Multidrug-Resistant Tuberculosis and Extensively Drug-*
829 *Resistant Tuberculosis.* Cold Spring Harb Perspect Med, 2015. **5**(9): p. a017863.
830 3. Husain, A.A., et al., *Current perspective in tuberculosis vaccine development for high TB endemic*
831 *regions.* Tuberculosis (Edinb), 2016. **98**: p. 149-58.
832 4. Eckhardt, M., et al., *A systems approach to infectious disease.* Nat Rev Genet, 2020. **21**(6): p.
833 339-354.
834 5. Davis, H.E., et al., *Long COVID: major findings, mechanisms and recommendations.* Nat Rev
835 Microbiol, 2023. **21**(3): p. 133-146.
836 6. Lippi, G., F. Sanchis-Gomar, and B.M. Henry, *COVID-19 and its long-term sequelae: what do we*
837 *know in 2023?* Pol Arch Intern Med, 2023. **133**(4).
838 7. Luies, L. and I. du Preez, *The Echo of Pulmonary Tuberculosis: Mechanisms of Clinical Symptoms*
839 *and Other Disease-Induced Systemic Complications.* Clin Microbiol Rev, 2020. **33**(4).
840 8. Loddenkemper, R., M. Lipman, and A. Zumla, *Clinical Aspects of Adult Tuberculosis.* Cold Spring
841 Harb Perspect Med, 2015. **6**(1): p. a017848.
842 9. Morley, J.E., D.R. Thomas, and M.M. Wilson, *Cachexia: pathophysiology and clinical relevance.*
843 Am J Clin Nutr, 2006. **83**(4): p. 735-43.
844 10. Chang, S.W., et al., *Gut hormones, appetite suppression and cachexia in patients with pulmonary*
845 *TB.* PLoS One, 2013. **8**(1): p. e54564.
846 11. Bisht, M.K., et al., *The cause-effect relation of tuberculosis on incidence of diabetes mellitus.*
847 Front Cell Infect Microbiol, 2023. **13**: p. 1134036.
848 12. Niazi, A.K. and S. Kalra, *Diabetes and tuberculosis: a review of the role of optimal glycemic*
849 *control.* J Diabetes Metab Disord, 2012. **11**(1): p. 28.
850 13. Jensen-Cody, S.O. and M.J. Potthoff, *Hepatokines and metabolism: Deciphering communication*
851 *from the liver.* Mol Metab, 2021. **44**: p. 101138.
852 14. Kumar, N.P., et al., *Acute Phase Proteins Are Baseline Predictors of Tuberculosis Treatment*
853 *Failure.* Front Immunol, 2021. **12**: p. 731878.
854 15. Quinton, L.J., A.J. Walkey, and J.P. Mizgerd, *Integrative Physiology of Pneumonia.* Physiol Rev,
855 2018. **98**(3): p. 1417-1464.
856 16. Shim, D., H. Kim, and S.J. Shin, *Mycobacterium tuberculosis Infection-Driven Foamy Macrophages*
857 *and Their Implications in Tuberculosis Control as Targets for Host-Directed Therapy.* Front
858 Immunol, 2020. **11**: p. 910.
859 17. Park, J.H., et al., *Understanding Metabolic Regulation Between Host and Pathogens: New*
860 *Opportunities for the Development of Improved Therapeutic Strategies Against Mycobacterium*
861 *tuberculosis Infection.* Front Cell Infect Microbiol, 2021. **11**: p. 635335.
862 18. Gago, G., L. Diacovich, and H. Gramajo, *Lipid metabolism and its implication in mycobacteria-host*
863 *interaction.* Curr Opin Microbiol, 2018. **41**: p. 36-42.
864 19. Wang, F., et al., *Organ-organ communication: The liver's perspective.* Theranostics, 2021. **11**(7):
865 p. 3317-3330.
866 20. Alper, C.A., et al., *Human C'3: evidence for the liver as the primary site of synthesis.* Science,
867 1969. **163**(3864): p. 286-8.

868 21. Zhou, Z., M.J. Xu, and B. Gao, *Hepatocytes: a key cell type for innate immunity.* Cell Mol
869 Immunol, 2016. **13**(3): p. 301-15.
870 22. Zhang, D., et al., *Important Hormones Regulating Lipid Metabolism.* Molecules, 2022. **27**(20).
871 23. Datta, D., et al., *Actionable mechanisms of drug tolerance and resistance in Mycobacterium*
872 *tuberculosis.* FEBS J, 2024.
873 24. Deb, C., et al., *A novel in vitro multiple-stress dormancy model for Mycobacterium tuberculosis*
874 *generates a lipid-loaded, drug-tolerant, dormant pathogen.* PLoS One, 2009. **4**(6): p. e6077.
875 25. Liu, Y., et al., *Immune activation of the host cell induces drug tolerance in Mycobacterium*
876 *tuberculosis both in vitro and in vivo.* J Exp Med, 2016. **213**(5): p. 809-25.
877 26. Samuels, A.N., et al., *Understanding the contribution of metabolism to Mycobacterium*
878 *tuberculosis drug tolerance.* Front Cell Infect Microbiol, 2022. **12**: p. 958555.
879 27. Santucci, P., et al., *Intracellular localisation of Mycobacterium tuberculosis affects efficacy of the*
880 *antibiotic pyrazinamide.* Nat Commun, 2021. **12**(1): p. 3816.
881 28. Wu, K.C. and C.J. Lin, *The regulation of drug-metabolizing enzymes and membrane transporters*
882 *by inflammation: Evidences in inflammatory diseases and age-related disorders.* J Food Drug
883 Anal, 2019. **27**(1): p. 48-59.
884 29. Wu, Z., et al., *Diagnosis and treatment of hepatic tuberculosis: report of five cases and review of*
885 *literature.* Int J Clin Exp Med, 2013. **6**(9): p. 845-50.
886 30. Turhan, N., et al., *Hepatic granulomas: a clinicopathologic analysis of 86 cases.* Pathol Res Pract,
887 2011. **207**(6): p. 359-65.
888 31. Hickey, A.J., et al., *A systematic review of hepatic tuberculosis with considerations in human*
889 *immunodeficiency virus co-infection.* BMC Infect Dis, 2015. **15**: p. 209.
890 32. Celton-Morizur, S., et al., *Polyploidy and liver proliferation: central role of insulin signaling.* Cell
891 Cycle, 2010. **9**(3): p. 460-6.
892 33. Jain, N., et al., *Mesenchymal stem cells offer a drug-tolerant and immune-privileged niche to*
893 *Mycobacterium tuberculosis.* Nat Commun, 2020. **11**(1): p. 3062.
894 34. Lerner, T.R., et al., *Mycobacterium tuberculosis cords within lymphatic endothelial cells to evade*
895 *host immunity.* JCI Insight, 2020. **5**(10).
896 35. Kalam, H., M.F. Fontana, and D. Kumar, *Alternate splicing of transcripts shape macrophage*
897 *response to Mycobacterium tuberculosis infection.* PLoS Pathog, 2017. **13**(3): p. e1006236.
898 36. Peyron, P., et al., *Foamy macrophages from tuberculous patients' granulomas constitute a*
899 *nutrient-rich reservoir for M. tuberculosis persistence.* PLoS Pathog, 2008. **4**(11): p. e1000204.
900 37. Beigier-Bompadre, M., et al., *Mycobacterium tuberculosis infection modulates adipose tissue*
901 *biology.* PLoS Pathog, 2017. **13**(10): p. e1006676.
902 38. Wolk, M. and M. Fedorova, *The lipid droplet lipidome.* FEBS Lett, 2024. **598**(10): p. 1215-1225.
903 39. Day, N.J., P. Santucci, and M.G. Gutierrez, *Host cell environments and antibiotic efficacy in*
904 *tuberculosis.* Trends Microbiol, 2023.
905 40. Fisher, C.D., et al., *Hepatic cytochrome P450 enzyme alterations in humans with progressive*
906 *stages of nonalcoholic fatty liver disease.* Drug Metab Dispos, 2009. **37**(10): p. 2087-94.
907 41. Almazroo, O.A., M.K. Miah, and R. Venkataramanan, *Drug Metabolism in the Liver.* Clin Liver Dis,
908 2017. **21**(1): p. 1-20.
909 42. Ahmed, S., et al., *Pharmacogenomics of Drug Metabolizing Enzymes and Transporters: Relevance*
910 *to Precision Medicine.* Genomics Proteomics Bioinformatics, 2016. **14**(5): p. 298-313.
911 43. Sotsuka, T., et al., *Association of isoniazid-metabolizing enzyme genotypes and isoniazid-induced*
912 *hepatotoxicity in tuberculosis patients.* In Vivo, 2011. **25**(5): p. 803-12.
913 44. Rocha-Granados, M.C., et al., *The social network: Impact of host and microbial interactions on*
914 *bacterial antibiotic tolerance and persistence.* Cell Signal, 2020. **75**: p. 109750.

45. Cosma, C.L., D.R. Sherman, and L. Ramakrishnan, *The secret lives of the pathogenic mycobacteria.* Annu Rev Microbiol, 2003. **57**: p. 641-76.
46. Bussi, C. and M.G. Gutierrez, *Mycobacterium tuberculosis infection of host cells in space and time.* FEMS Microbiol Rev, 2019. **43**(4): p. 341-361.
47. Lu, J.F., et al., *GDF15 is a major determinant of ketogenic diet-induced weight loss.* Cell Metab, 2023. **35**(12): p. 2165-2182 e7.
48. Seiler, P., et al., *Limited mycobacterial infection of the liver as a consequence of its microanatomical structure causing restriction of mycobacterial growth to professional phagocytes.* Infect Immun, 2001. **69**(12): p. 7922-6.
49. Hess, S., et al., *In vivo partial reprogramming by bacteria promotes adult liver organ growth without fibrosis and tumorigenesis.* Cell Rep Med, 2022. **3**(11): p. 100820.
50. Arnett, E., et al., *PPARgamma is critical for Mycobacterium tuberculosis induction of Mcl-1 and limitation of human macrophage apoptosis.* PLoS Pathog, 2018. **14**(6): p. e1007100.
51. Rajaram, M.V., et al., *Mycobacterium tuberculosis activates human macrophage peroxisome proliferator-activated receptor gamma linking mannose receptor recognition to regulation of immune responses.* J Immunol, 2010. **185**(2): p. 929-42.
52. Díaz, A., et al., *Studies on the contribution of PPAR Gamma to tuberculosis physiopathology.* Front Cell Infect Microbiol, 2023. **13**: p. 1067464.
53. Bechmann, L.P., et al., *The interaction of hepatic lipid and glucose metabolism in liver diseases.* J Hepatol, 2012. **56**(4): p. 952-64.
54. Lovewell, R.R., C.M. Sassetti, and B.C. VanderVen, *Chewing the fat: lipid metabolism and homeostasis during M. tuberculosis infection.* Curr Opin Microbiol, 2016. **29**: p. 30-6.
55. Rey-Bedon, C., et al., *CYP450 drug inducibility in NAFLD via an in vitro hepatic model: Understanding drug-drug interactions in the fatty liver.* Biomed Pharmacother, 2022. **146**: p. 112377.
56. Dookie, N., et al., *Evolution of drug resistance in Mycobacterium tuberculosis: a review on the molecular determinants of resistance and implications for personalized care.* J Antimicrob Chemother, 2018. **73**(5): p. 1138-1151.
57. Barreto, E.A., et al., *COVID-19-related hyperglycemia is associated with infection of hepatocytes and stimulation of gluconeogenesis.* Proc Natl Acad Sci U S A, 2023. **120**(21): p. e2217119120.
58. Mercado-Gomez, M., et al., *The spike of SARS-CoV-2 promotes metabolic rewiring in hepatocytes.* Commun Biol, 2022. **5**(1): p. 827.
59. Hazlehurst, J.M., et al., *Non-alcoholic fatty liver disease and diabetes.* Metabolism, 2016. **65**(8): p. 1096-108.
60. Dharmalingam, M. and P.G. Yamasandhi, *Nonalcoholic Fatty Liver Disease and Type 2 Diabetes Mellitus.* Indian J Endocrinol Metab, 2018. **22**(3): p. 421-428.
61. Toda, G., et al., *Preparation and culture of bone marrow-derived macrophages from mice for functional analysis.* STAR Protoc, 2021. **2**(1): p. 100246.
62. Bligh, E.G. and W.J. Dyer, *A rapid method of total lipid extraction and purification.* Can J Biochem Physiol, 1959. **37**(8): p. 911-7.

958 **Main figure legends:**

959 **Figure 1: Presence of Mtb in human pulmonary tuberculosis patients: (A)**
960 Hematoxylin and eosin (H and E) staining of the human autopsied liver tissue sections
961 showing the presence of granuloma-like structure in the Mtb infected liver. **(B)** Acid-fast
962 staining showing the presence of Mtb in the liver section of pulmonary TB patients.
963 (arrows point to the presence of Mtb in the enlarged image) **(C-D)** Auramine O-
964 Rhodamine B (A-O) staining and fluorescence in-situ hybridization (FISH) with Mtb
965 specific 16s rRNA primer further confirms the presence of Mtb in human liver tissue
966 sections. Data shown here is a representative of 5 autopsied specimens having Mtb
967 infection. **(E).** Dual staining of β-actin (green) and Ag85B (red) using respective antibodies
968 shows the presence of Mtb in hepatocytes of human biopsied liver sections.

969 **Figure 2: Involvement of the liver and hepatocytes in a mouse aerosol model of**
970 **Mtb infection**. **(A).** Schematic denoting the flow of experimental set up of studying the
971 liver at tissue level and cellular level (generated by Biorender.com). **(B)** C57BL/6 mice
972 were infected with 200 CFU of H37Rv through the aerosol route and the bacterial burden
973 of the lung and liver was enumerated at different time points post-infection in lung and
974 spleen **(C).** Alexa Fluor 488 Phalloidin and DAPI staining of uninfected and infected lungs
975 at 8 weeks post-infection. Images were taken in 20X, and 40 X magnification as
976 mentioned (scale bar is 20 μm). **(D).** Immunofluorescence staining of Alexa Fluor 488
977 Phalloidin, DAPI, and Ag85B in the infected mice liver at 8 weeks post-infection shows
978 the presence of Ag85B signals within hepatocytes (magnified image) (scale bar is 20 μm).
979 **(E)**. Isolated primary hepatocytes stained with phalloidin green and DAPI show the typical
980 polygonal shape with binucleated morphology. **(F).** Anti-asialoglycoprotein receptor

981 (ASGR1) antibody staining specifically stains primary hepatocytes isolated from infected
982 mice as validated by the contour plot in flow cytometry. (**G).** Anti-asialoglycoprotein
983 receptor (ASGR1) antibody staining specifically stains primary hepatocytes isolated from
984 mice as visualized through confocal microscopy. **(H).** Primary hepatocytes were isolated
985 from the infected mice, lysed and CFU enumeration was done at the mentioned time
986 points. **(I).** Ag85B staining of cultured primary hepatocytes, isolated from mice at 8 weeks
987 post Mtb infection. (scale bar is 20 µm). **(G)**. Animal litter size (n)= 6-7 mice in each group.

988 **Figure 3: Mtb uses hepatocytes as a replicative niche: (A and B)** Representative
989 microscopic images showing the infection of primary hepatocytes (PHCs), AML-12,
990 HepG2, and Huh-7 with labelled Mtb-*H37Rv* strains and subsequent quantification of
991 percentage infectivity in the respective cell types. RAW 264.7, THP-1 and murine BMDMs
992 were used as macrophage controls. The scale bar in all images is 10 µm except in HepG2,
993 which is 5 µm **(C)** CFU enumeration of Mtb-*H37Rv* in different hepatic cell lines. **(D and**
994 **E)** Representative confocal microscopy images of Mtb-GFP-*H37Rv* infected PHCs at the
995 respective time points post-infection and bar blot depicting mean fluorescent intensity
996 (MFI) / cell at the respective time points. **(F and G)** Representative confocal microscopy
997 images of Mtb-*H37Rv***-**GFP infected HepG2 at the respective time points post-infection
998 and bar blot depicting MFI/cell at the respective time points**,** n= 4 independent
999 experiments, with each dot representing 5 fields of 30-60 cells. Scale bar 10 µm. Growth
1000 kinetics of Mtb-*H37Rv* in **(H)** Fold change of growth rate of Mtb within HepG2, PHCs,
1001 RAW 264.7, THP-1 and BMDMs.

1002 **Figure 4: RNA sequence analysis of infected and sorted hepatocytes at 0 hours and**
1003 **48 hours post-infection (A)** Experimental setup for infection of HepG2 with Mb-*H37Rv*-

1004 mCherry at 10 MOI with histogram of mCherry signals at 0- and 48-hours post-infection(
1005 Schematic depicting experimental set up generated with Biorender.com) **(B)** Principal
1006 component analysis (PCA) plot illustrating the HepG2 transcriptome, identified through
1007 global transcriptomic analysis of 0 hours uninfected and infected and 48 hours uninfected
1008 and infected. **(C)** GO pathway enrichment analysis was done for DEGs with adjusted p-
1009 value < 0.05 at 0- and 48-hours post-infection. The bubble plot depicts the enrichment of
1010 pathways on the mentioned time points post-infection, where the coordinate on the x-axis
1011 represents the gene ratio, the bubble size represents the gene count and colour
1012 represents the p-value. **(D and E)** Volcano plot depicting the fold change of different
1013 genes in 0 hours and 48 hours post-infection, the red dots represent the significantly
1014 upregulated and downregulated genes.

1015 **Figure 5**: **Increased fatty acid biogenesis drives Mtb growth in hepatocytes**: **(A)**
1016 Increased number of LDs/cells in HepG2 and PHCs post-Mtb infection **(B).** Quantification
1017 of the number of lipid droplets in the infected HepG2 and PHCs with their uninfected
1018 control, 50-70 cells were analyzed from 3 independent experiments. **(C).** Increase in the
1019 BODIPY intensity at different days post-infection in infected hepatocytes **(D)**. A high
1020 degree of colocalization of Mtb-*H37Rv*-GFP (green) with lipid droplets (red) within PHCs
1021 **(E)** Mass spectrometric quantification of the different species of DAGs, TAGs, and
1022 cholesterol esters in the Mtb infected hepatocytes. **(F)**. Confocal images showing puncta
1023 of fluorescently labelled fatty acid in Mtb derived from metabolically labelled (with BODIPY
1024 558/568 C_{12}) HepG2**.** Relative CFU of Mtb under the administration of different inhibitors
1025 of the lipid metabolic pathway in **(G)** PHCs **(H)** HepG2 and **(I)** THP-1. Representative data
1026 from 3 independent experiments. Data were analyzed using the two-tailed unpaired

1027 Student's t-test in B and one-way ANOVA in C, F, G, and H.*p < 0.05, **p < 0.005, ***p <
1028 0.0005, ****p < 0.0001. ns=non-significant.

1029 **Figure 6: PPARγ driven lipid biogenesis drives Mtb growth in hepatocytes: (A)** Heat
1030 map showing the fold change of the genes involved in the lipid biosynthesis and LD
1031 biogenesis in liver across weeks 2, 4 and 8, post infection. **(B)** Kinetic increase in the
1032 gene expression of *Pparγ* transcript levels across different weeks post infection **(C)**
1033 Immunoblot showing increased PPARγ in PHCs (MOI: 10) at 5 ,24 and 48 hours post-
1034 infection. **(D)** Bar plot showing the increased band intensity of PPARγ in the infected
1035 PHCs at the mentioned time points. **(E)** Representative confocal microscopy images
1036 showing HepG2 infected with Mtb-mCherry-*H37Rv* and treated with GW9662 and
1037 rosiglitazone **(F)** MFI/cell of in Mtb-mCherry-*H37Rv* DMSO treated, GW9662 and
1038 rosiglitazone treated HepG2 cells. **(G)** Representative confocal images of uninfected,
1039 infected, GW9662 and rosiglitazone treated infected HepG2 showing changes in the
1040 number of LDs. **(H)** Plot depicting the quantification of LDs/cell in the mentioned
1041 conditions. Representative data from n=4 biological replicates. Data were analysed by
1042 using the two tailed unpaired Student's t test in D and by one way ANOVA in B, F and H.
1043 *p < 0.05, **p < 0.005, ***p < 0.0005, ****p < 0.0001, ns=non-significant

1044 **Figure 7: Hepatocytes provide a drug-tolerant niche to Mtb: (A).** Experimental
1045 scheme of deducting the percentage drug tolerance in hepatocytes (generated with
1046 iorender.com) **(B).** Percentage tolerance of Mtb-*H37Rv* against Rifampicin within RAW
1047 264.7, PHCs and HepG2 at different time points post-infection. **(C).** Percentage tolerance
1048 of Mtb-H37Rv against Isoniazid within RAW 264.7, PHCs, and HepG2 at different time
1049 points post-infection. Representative data from 3 independent experiments. **(D).**

1050 Percentage tolerance of Mtb-*H37Rv* against rifampicin within BMDMs, PHCs, and HepG2
1051 as measured microscopically (**E).** Percentage tolerance of Mtb-H37Rv against isoniazid
1052 within BMDMs, PHCs, and HepG2 measured microscopically. Representative data from
1053 3 independent experiments. Each dot represents a single field having more than 4
1054 infected cells. 20 such fields were analyzed **(F)**. Transcript levels of the various DMEs
1055 involved in Rifampicin and Isoniazid metabolism in mice liver, 8 weeks post-infection (n=4
1056 mice), the fold change has been calculated by considering the expression in the
1057 uninfected mice to be 1. Data were analyzed by using 2-way ANOVA in (B) and (C), one-
1058 way ANOVA in (D) and (E) and the two-tailed unpaired Student's t-test in (F) and
1059 Representative data from n=4 biological replicates *p < 0.05, **p < 0.005, ***p < 0.0005,
1060 ****p < 0. 0001.ns=non-significant.

1061

1062

1063

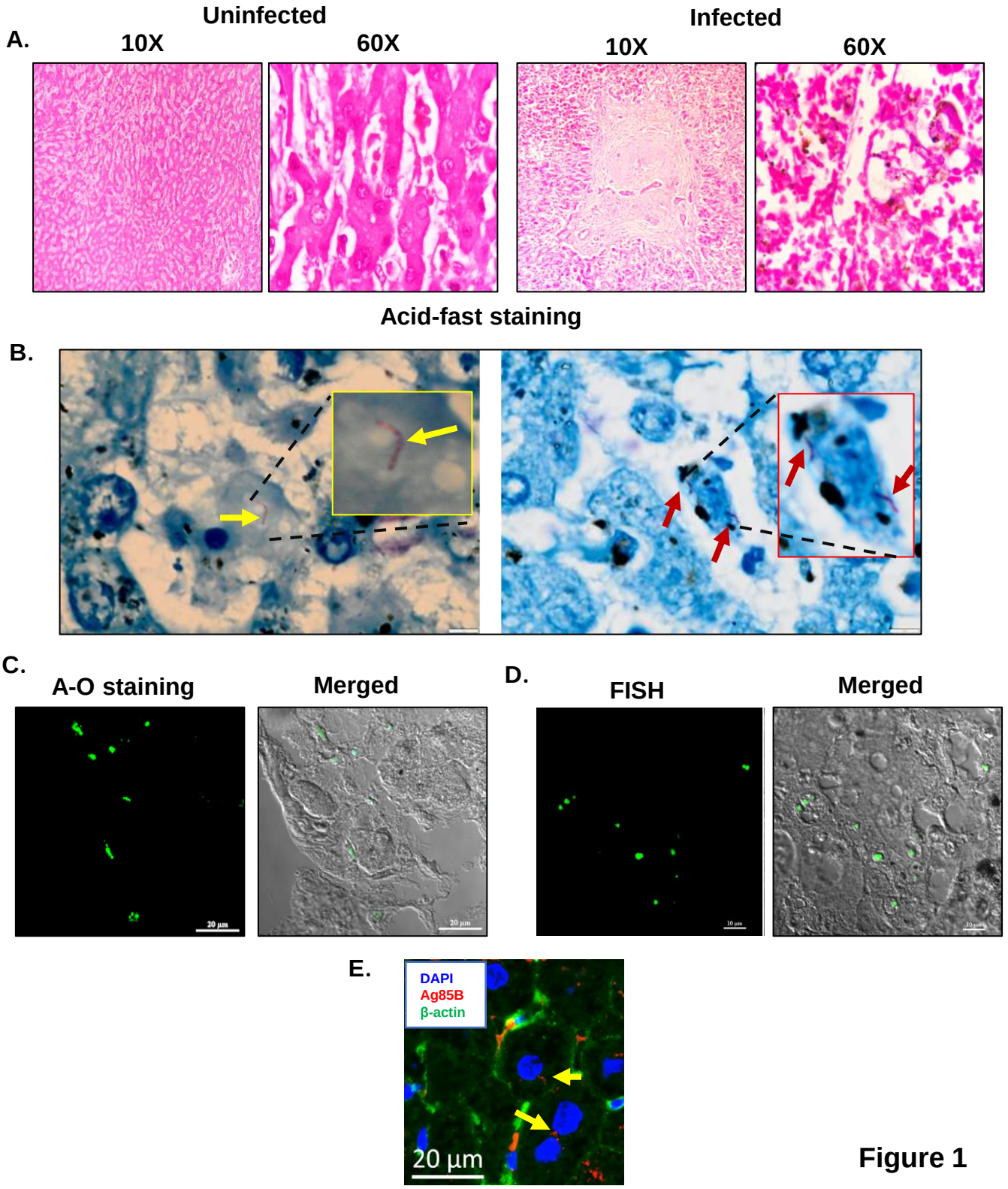
A.
Uninfected
10X
60X
Infected
10X
60X
Acid-fast staining
B.
C.
A-O staining
Merged
D.
FISH
Merged
E.
DAPI
Ag85B
β-actin
20 µm

Figure 1

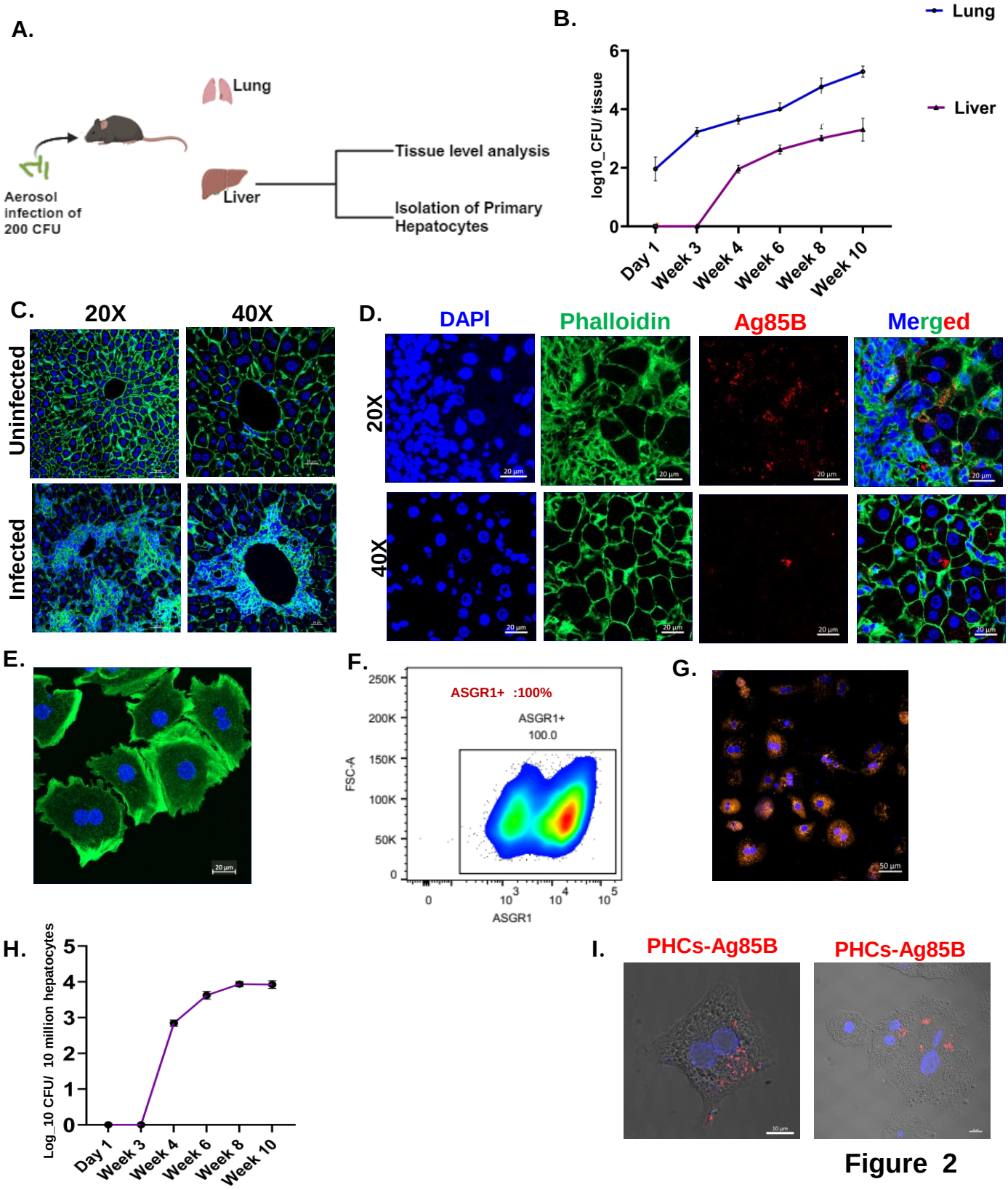
A.
Lung
Aerosol infection of 200 CFU
Liver
Tissue level analysis
Isolation of Primary Hepatocytes
B.
Lung
Liver
log10_CFU/ tissue
0
2
4
6
Day 1
Week 3
Week 4
Week 6
Week 8
Week 10
C.
20X
40X
Uninfected
Infected
D.
DAPI
Phalloidin
Ag85B
Merged
20X
40X
20 µm
E.
20 µm
F.
ASGR1+ :100%
ASGR1+
100.0
FSC-A
250K
200K
150K
100K
50K
0
ASGR1
G.
50 µm
H.
Log_10 CFU/ 10 million hepatocytes
0
1
2
3
4
5
Day 1
Week 3
Week 4
Week 6
Week 8
Week 10
I.
PHCs-Ag85B
PHCs-Ag85B

Figure 2

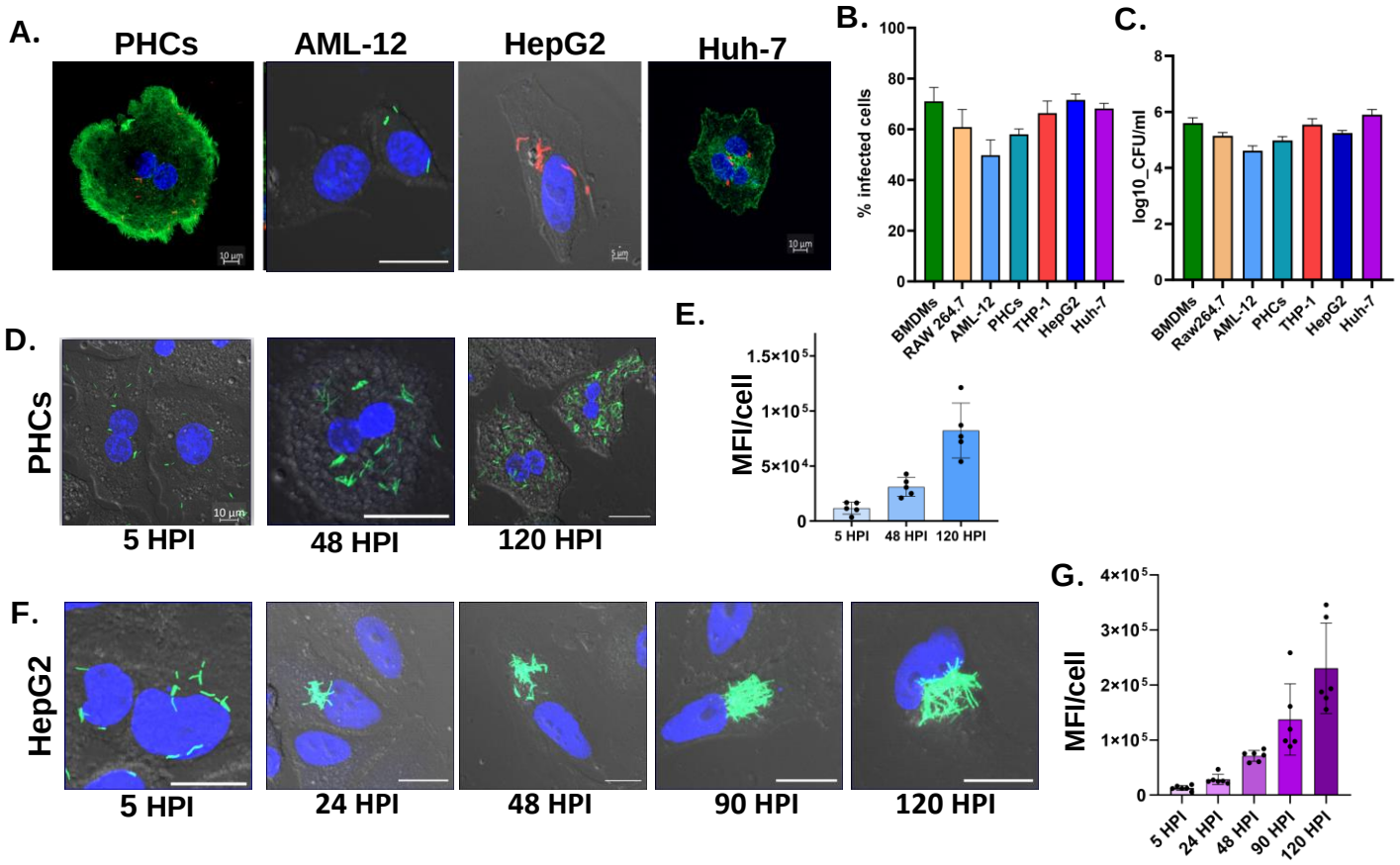
A.
PHCs
AML-12
HepG2
Huh-7
B.
% infected cells
BMDMs
RAW 264.7
AML-12
PHCs
THP-1
HepG2
Huh-7
C.
log10_CFU/ml
BMDMs
Raw264.7
AML-12
PHCs
THP-1
HepG2
Huh-7
D.
PHCs
5 HPI
48 HPI
120 HPI
E.
MFI/cell
5 HPI
48 HPI
120 HPI
F.
HepG2
5 HPI
24 HPI
48 HPI
90 HPI
120 HPI
G.
MFI/cell
5 HPI
24 HPI
48 HPI
90 HPI
120 HPI

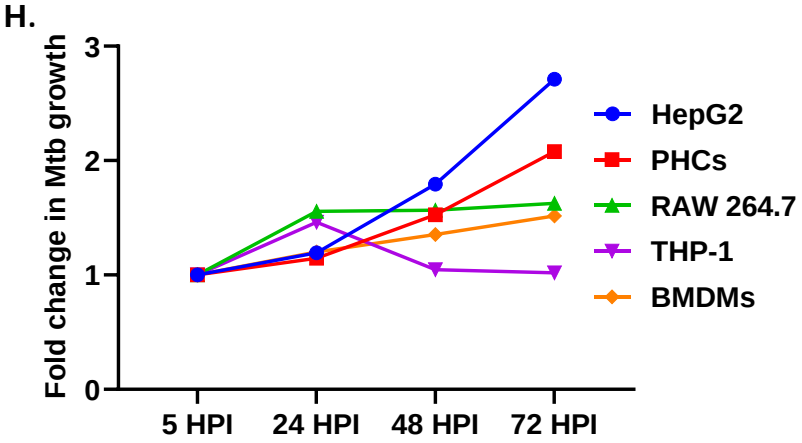
H.
Fold change in Mtb growth
5 HPI
24 HPI
48 HPI
72 HPI
HepG2
PHCs
RAW 264.7
THP-1
BMDMs

Figure 3

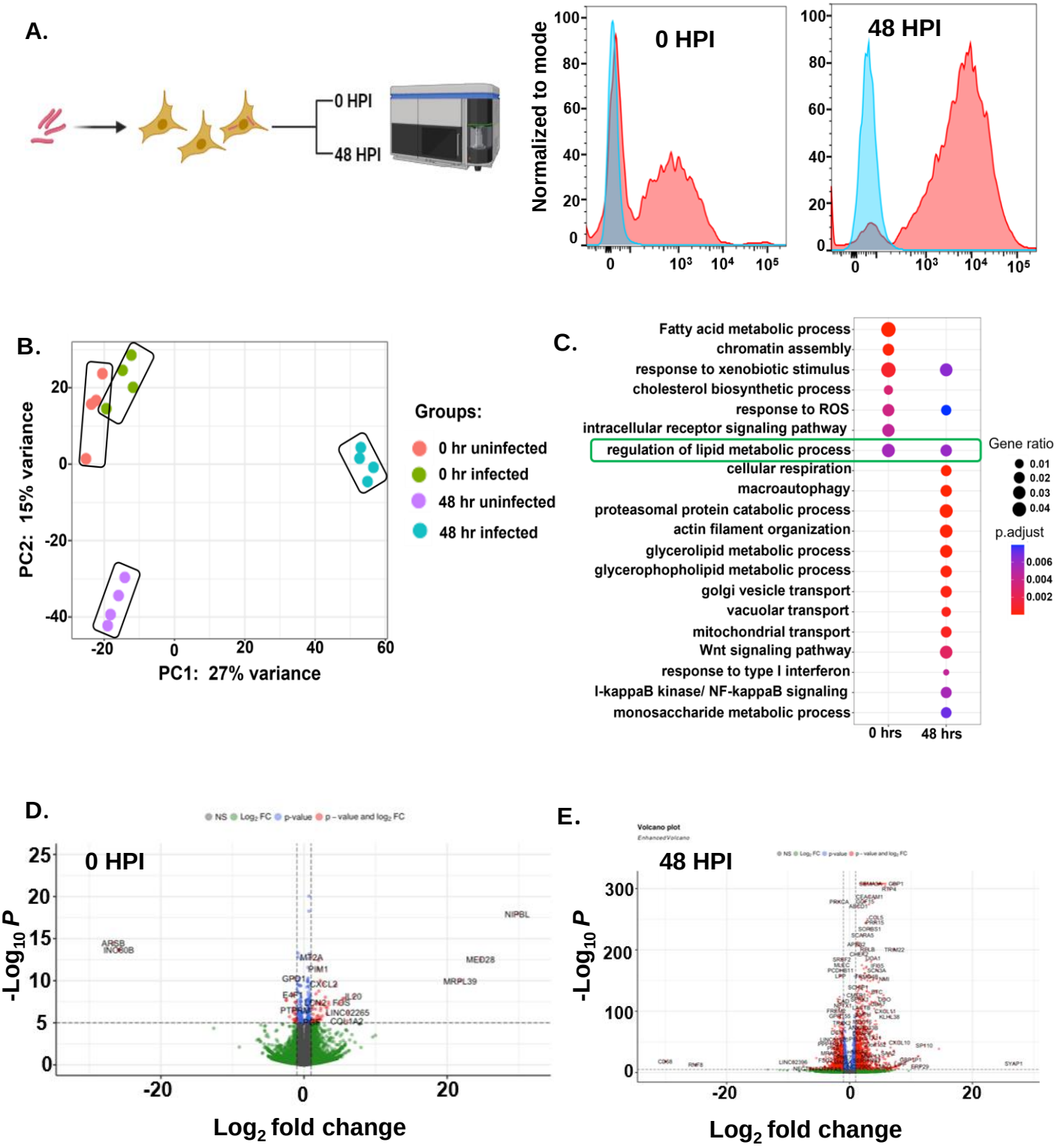
A.
0 HPI
48 HPI
Normalized to mode
0 HPI
48 HPI
B.
PC2: 15% variance
PC1: 27% variance
Groups:
0 hr uninfected
0 hr infected
48 hr uninfected
48 hr infected
C.
Fatty acid metabolic process
chromatin assembly
response to xenobiotic stimulus
cholesterol biosynthetic process
response to ROS
intracellular receptor signaling pathway
regulation of lipid metabolic process
cellular respiration
macroautophagy
proteasomal protein catabolic process
actin filament organization
glycerolipid metabolic process
glycerophopholipid metabolic process
golgi vesicle transport
vacuolar transport
mitochondrial transport
Wnt signaling pathway
response to type I interferon
I-kappaB kinase/ NF-kappaB signaling
monosaccharide metabolic process
0 hrs
48 hrs
Gene ratio
0.01
0.02
0.03
0.04
p.adjust
0.006
0.004
0.002
D.
0 HPI
-Log10 P
Log2 fold change
NIPBL
MED28
MRPL39
E.
Volcano plot
48 HPI
-Log10 P
Log2 fold change

Figure 4

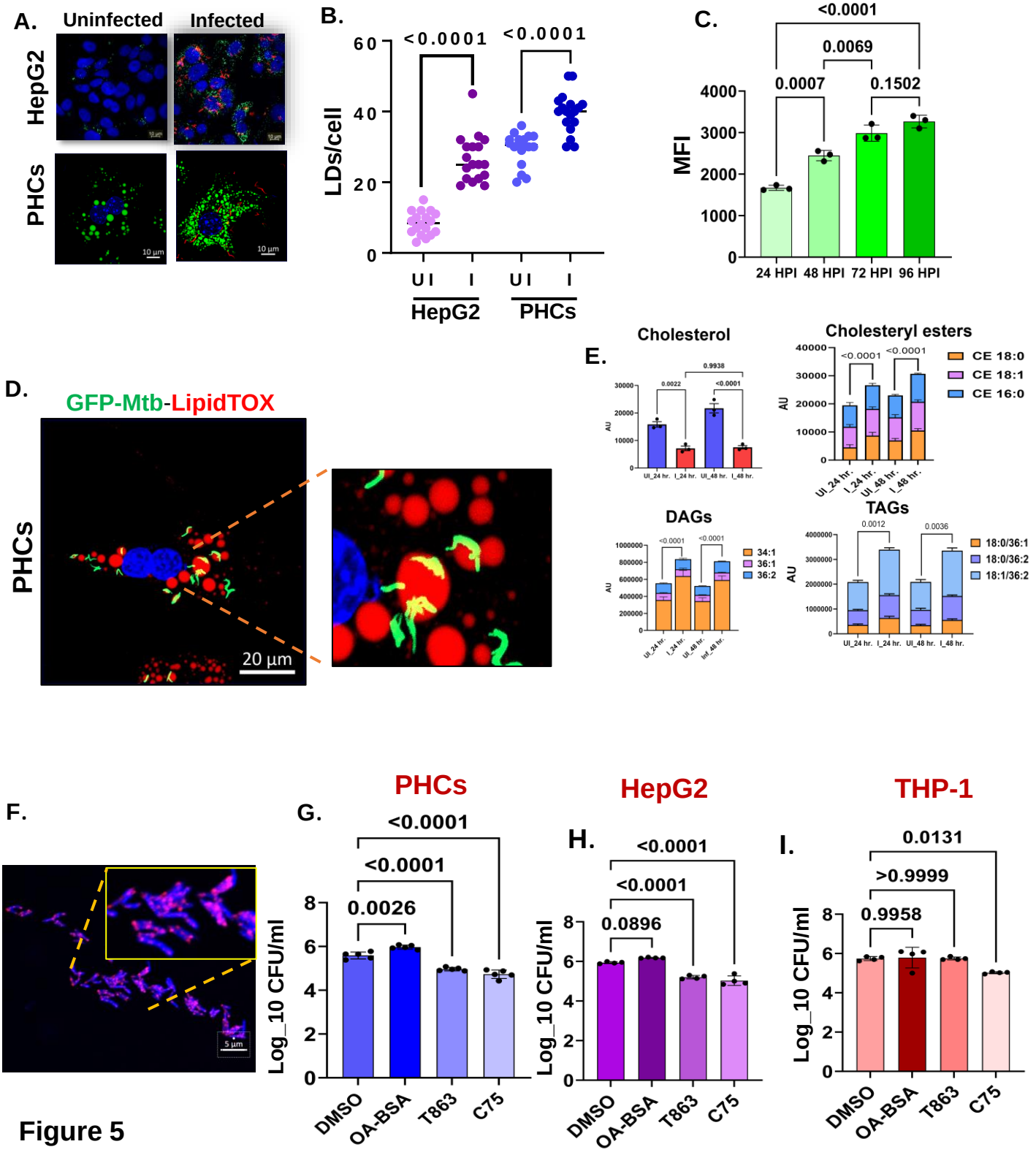
A.
Uninfected
Infected
HepG2
PHCs
10 µm
B.
LDs/cell
<0.0001
<0.0001
U I
I
U I
I
HepG2
PHCs
C.
MFI
<0.0001
0.0069
0.0007
0.1502
24 HPI
48 HPI
72 HPI
96 HPI
D.
GFP-Mtb-LipidTOX
PHCs
20 µm
E.
Cholesterol
Cholesteryl esters
CE 18:0
CE 18:1
CE 16:0
DAGs
34:1
36:1
36:2
TAGs
18:0/36:1
18:0/36:2
18:1/36:2
AU
F.
5 µm
G.
PHCs
H.
HepG2
I.
THP-1
Log_10 CFU/ml
DMSO
OA-BSA
T863
C75

Figure 5

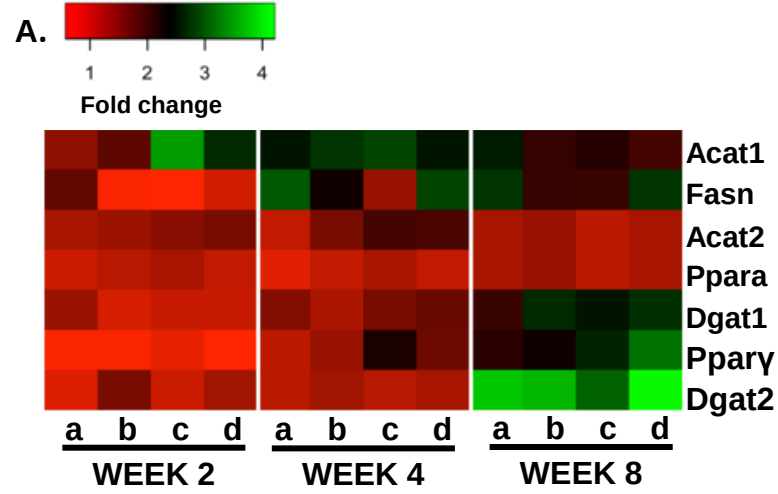
A.
1
2
3
4
Fold change
Acat1
Fasn
Acat2
Ppara
Dgat1
Pparγ
Dgat2
a b c d
a b c d
a b c d
WEEK 2
WEEK 4
WEEK 8

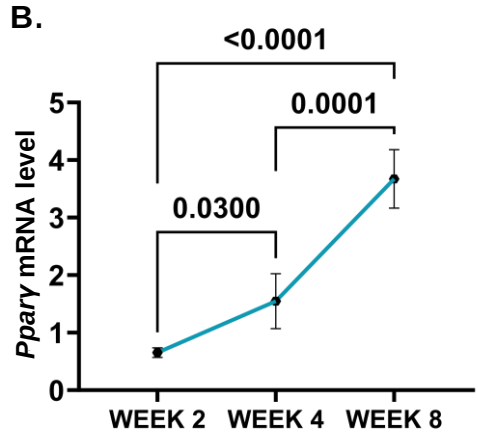
B.
<0.0001
0.0001
0.0300
Ppary mRNA level
0
1
2
3
4
5
WEEK 2
WEEK 4
WEEK 8

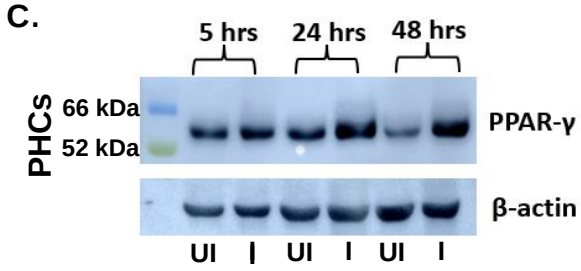
C.
5 hrs
24 hrs
48 hrs
PHCs
66 kDa
52 kDa
PPAR-γ
β-actin
UI
I
UI
I
UI
I

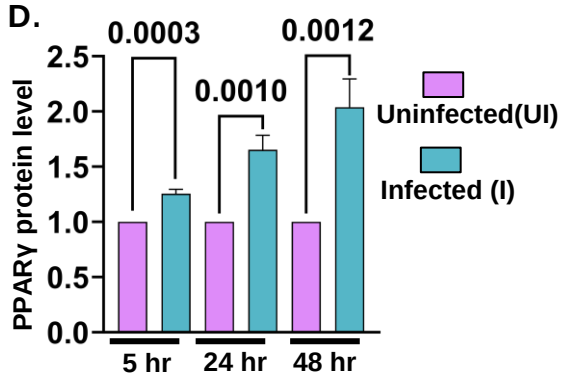
D.
0.0003
0.0010
0.0012
PPARγ protein level
0.0
0.5
1.0
1.5
2.0
2.5
Uninfected(UI)
Infected (I)
5 hr
24 hr
48 hr

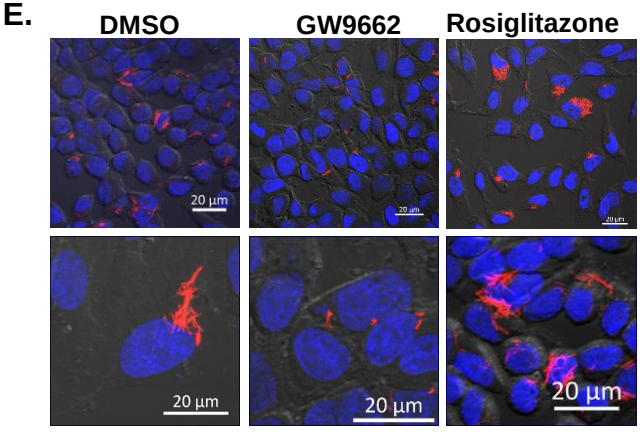
E.
DMSO
GW9662
Rosiglitazone
20 µm
20 µm
20 µm
20 µm

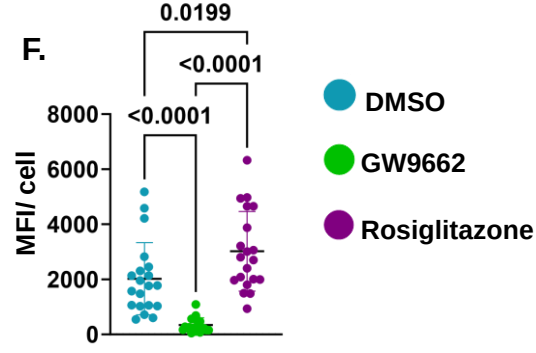
F.
0.0199
<0.0001
<0.0001
MFI/ cell
0
2000
4000
6000
8000
DMSO
GW9662
Rosiglitazone

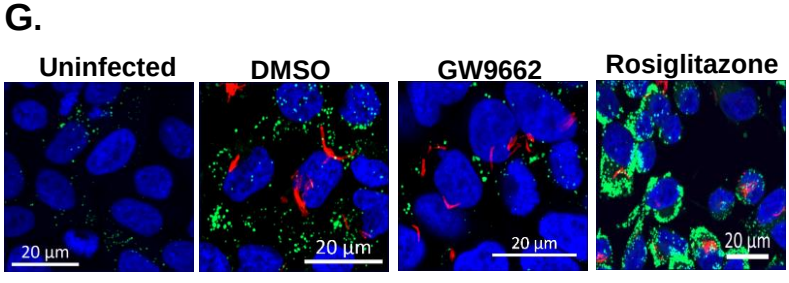
G.
Uninfected
DMSO
GW9662
Rosiglitazone
20 µm
20 µm
20 µm
20 µm

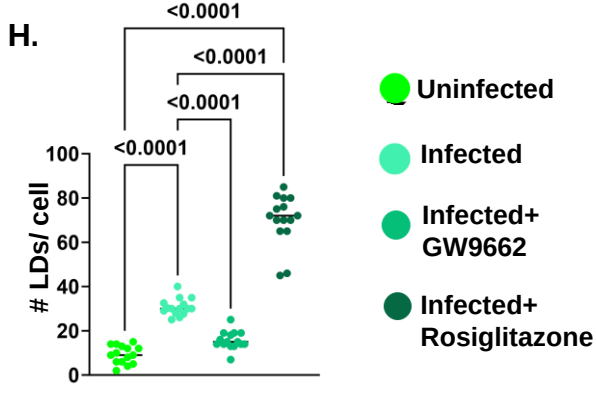
H.
<0.0001
<0.0001
<0.0001
<0.0001
LDs/ cell
0
20
40
60
80
100
Uninfected
Infected
Infected+ GW9662
Infected+ Rosiglitazone

Figure 6

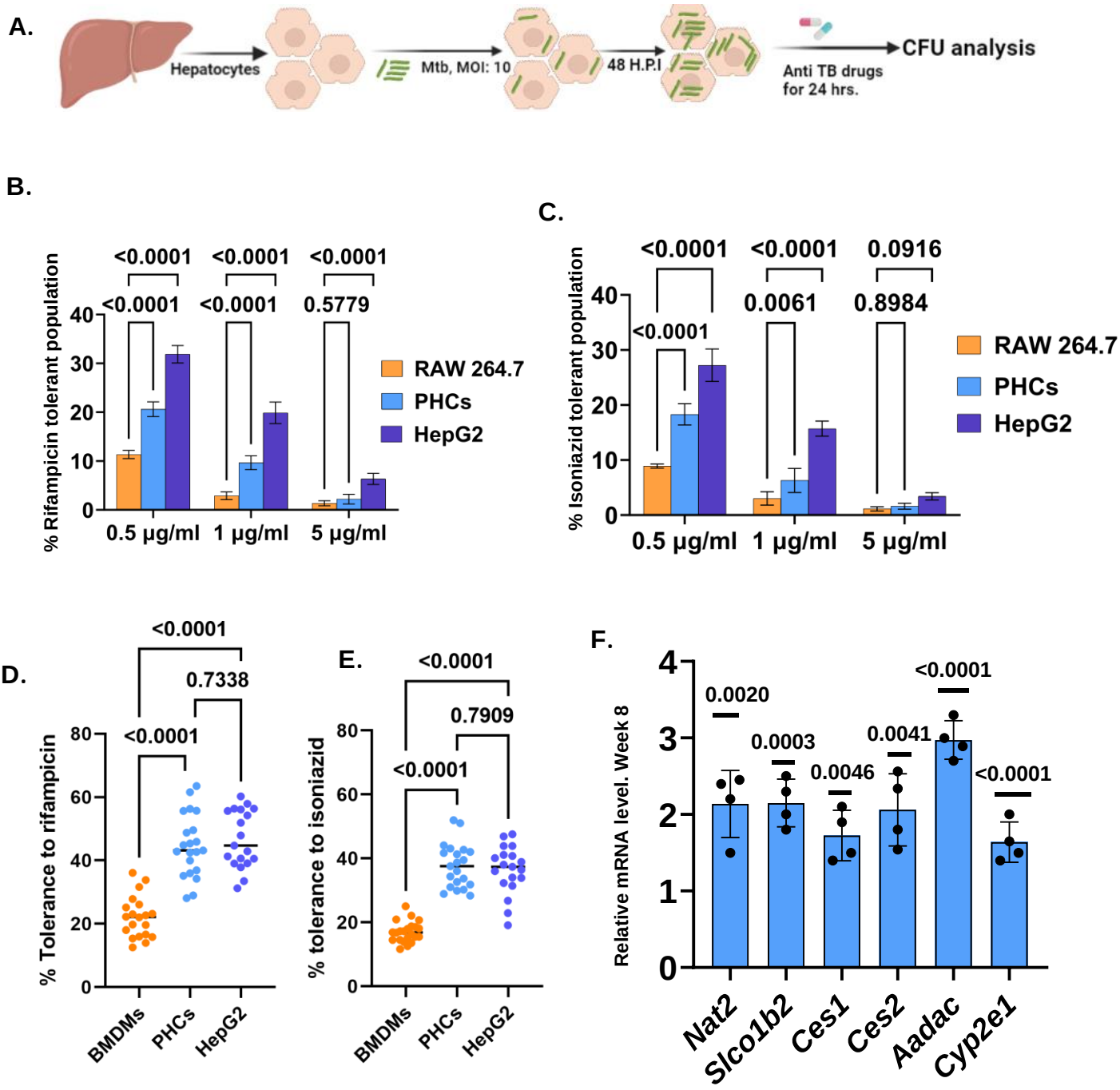
A.
Hepatocytes
Mtb, MOI: 10
48 H.P.I
Anti TB drugs
for 24 hrs.
CFU analysis
B.
% Rifampicin tolerant population
<0.0001
<0.0001
<0.0001
<0.0001
<0.0001
0.5779
0.5 µg/ml
1 µg/ml
5 µg/ml
RAW 264.7
PHCs
HepG2
C.
% Isoniazid tolerant population
<0.0001
<0.0001
0.0916
<0.0001
0.0061
0.8984
0.5 µg/ml
1 µg/ml
5 µg/ml
RAW 264.7
PHCs
HepG2
D.
% Tolerance to rifampicin
<0.0001
0.7338
<0.0001
BMDMs
PHCs
HepG2
E.
% tolerance to isoniazid
<0.0001
0.7909
<0.0001
BMDMs
PHCs
HepG2
F.
Relative mRNA level. Week 8
0.0020
0.0003
0.0046
0.0041
<0.0001
<0.0001
Nat2
Slco1b2
Ces1
Ces2
Aadac
Cyp2e1

Figure 7